

Investigation of atomically thin films: state of the art

K V Larionov, P B Sorokin

DOI: <https://doi.org/10.3367/UFNe.2020.03.038745>

Contents

1. Introduction	28
2. Monolayer films of metals	29
3. Monolayer films of metal compounds	33
3.1 Ionic graphitization effect; 3.2 2D monoxides of transition metals; 3.3 2D monocarbides of transition metals	
4. Two-dimensional films based on elements of groups 13–16	37
4.1 Silicene and germanene; 4.2 Borophene; 4.3 Two-dimensional films of other elements of groups 13–16	
5. Conclusion	45
References	45

Abstract. The review is devoted to the current state of research in one of the topical areas of the physics and chemistry of two-dimensional materials — the study of atomically thin films. The structure and properties of atomically thin monoelemental films, such as 2D iron, gold, and lithium, as well as silicene, germanene, borophene, etc., are described in detail. Two-dimensional films of metallic compounds like iron, copper, and zinc oxides and iron, cobalt, and copper carbides are considered. The main approaches to the stabilization of monoatomic films inside pores or between layers of other 2D materials are presented, and the exfoliation mechanism of ionic-covalent films with a polar surface into weakly bounded monolayers is described.

Keywords: two-dimensional monoelemental films, graphene, iron (Fe), molybdenum (Mo), gold (Au), lithium (Li), silicene, germanene, borophene, two-dimensional films of metallic compounds, molybdenum disulfide (MoS_2), zinc oxide (ZnO), copper oxide (CuO), iron carbide (FeC), cobalt carbide (CoC)

1. Introduction

The isolation [1] and subsequent detailed study of graphene [1–4] have shown its significant prospects and potential for use in a wide range of technologies, such as composite materials, low-dimensional catalysts, touch screens, conductive ink, electronic paper, and organic light-emitting diodes.

In 10–20 years, the introduction of graphene-based transistors and other logic units is expected [5].

The main obstacles to the wide use of graphene in electronics are the requirements of high quality of the synthesized atomic structure and the absence of a bandgap. The latter is a fundamental problem, to which no universal solution has been found yet. Each of the approaches proposed, e.g., functionalization, the introduction of defects into the structure, or graphene splitting into separate ribbons, has its drawbacks [6]. Indeed, the chemical adsorption of atoms on graphene leads to a change in the hybridization of carbon atoms from sp^2 to sp^3 accompanied by destruction of the π -system responsible for graphene conductivity. The proposed partial functionalization by forming hydrated [7] or fluorinated [8] regions (in a limiting case, separate periodically arranged chains of hydrogen [9–11]) solves the problem, because a bandgap opens between the regions due to the dimensional effect. However, in spite of experimental confirmation of the effect [12], this technique requires adsorption with atomic precision, which at present is hardly a solvable problem [13].

Using monolayers of different compositions can be an alternative way, especially as pioneering study [1] has demonstrated the flexibility of the micromechanical exfoliation approach for obtaining planar two-dimensional structures from any crystals with weakly bound layers (Fig. 1). The resulting materials have a planar structure as thin as one or a few atomic layers, whereas the lateral size can exceed a few micrometers. The atomic-size thickness, quantum dimensional effects, and high anisotropy of the optical properties of two-dimensional nanomaterials, as well as prospects of their application [14], have continuously attracted great interest of the world scientific community.

Studies on finding new quasi-2D films turned out to be so efficient that up to 2020 they numbered a few hundred. This led to a paradoxical situation of a lack of resources in the scientific community sufficient for their thorough investigation [15]. Moreover, the latest theoretical studies predict the possibility of five to six thousand more compounds in a quasi-2D state [16, 17], which ultimately makes 2D materials one of the most vast and poorly studied areas of up-to-date materials science (Fig. 2).

K V Larionov⁽¹⁾, P B Sorokin⁽²⁾

National University of Science and Technology MISIS,
Leninskii prosp. 4, 119049 Moscow, Russian Federation;
Moscow Institute of Physics and Technology
(National Research University),
Institutskii per. 9, 141701 Dolgoprudny, Moscow region,
Russian Federation
E-mail: ⁽¹⁾ konstantin.larionov@phystech.edu, ⁽²⁾ PBSorokin@misis.ru

Received 15 January 2020, revised 17 March 2020

Uspekhi Fizicheskikh Nauk 191 (1) 30–51 (2021)

Translated by V L Derbov

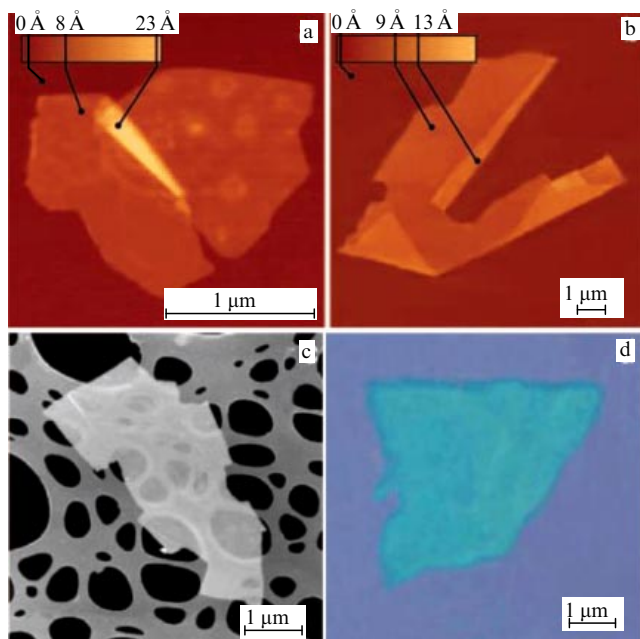


Figure 1. Atomically thin films, obtained in Ref. [1] by micromechanical exfoliation: (a) NbSe₂, (b) graphene, (c) Bi₂Sr₂CaCu₂O_x, (d) MoS₂. Images are obtained (a, b) by atomic-force microscopy, (c) using scanning electron microscopy, (d) by means of optical microscopy.

The aim of the present review is to inform a wide range of readers about the current state of materials science in the field of noncarbon 2D structures. However, because of the great number of discovered and predicted two-dimensional crystals mentioned above, the discussion is focused on atomically thin films only. This gives rise to a certain difficulty in classifying the compounds described; for example, whether the films of phosphorene [18] or silicene [19] are atomically thin or not? Indeed, both structures have a thickness of a single atom and differ only by the degree of lattice corrugation. Therefore, a criterion should be introduced, according to which the

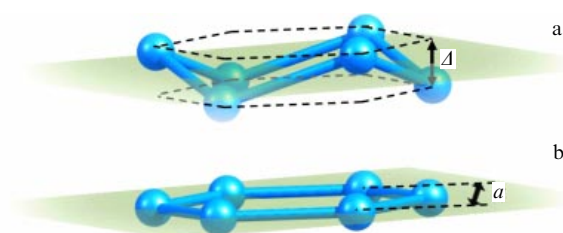


Figure 3. Corrugated (a) and planar (b) monolayer structures.

present review will consider only those compounds with the corrugation degree (the out-of-plane displacement of atoms Δ) much smaller than the lattice parameter of the crystal a , i.e., $\Delta \ll a$ (Fig. 3). Notably, this criterion excludes phosphorene from consideration, but requires describing silicene and other allied materials.

The review consists of three main sections. Section 2 considers single-layer films consisting exclusively of metal atoms (Fe, Au, etc.) and the possibility of their stabilization using other two-dimensional materials (mainly graphene). Section 3 presents a detailed description of various two-dimensional metal compounds, in particular, oxides and carbides of transition metals. Section 4 is devoted to films consisting of elements of groups 13–16 of the periodic table: silicene, borophene, and allied materials.

2. Monolayer films of metals

With the progress in the field of two-dimensional materials, the number of crystalline compounds with a layered structure that allows exfoliation and isolation of two-dimensional layers has been quickly exhausted. Therefore, researchers began to pay attention to nonlayered compounds and to try stabilizing them in the form of superthin films. These studies led to obtaining new unusual phases of 2D ice [20], silica [21], diamond [22], hematite [23], etc., as well as entire classes of novel materials, e.g., MXenes [24]. The possibility of stabiliz-

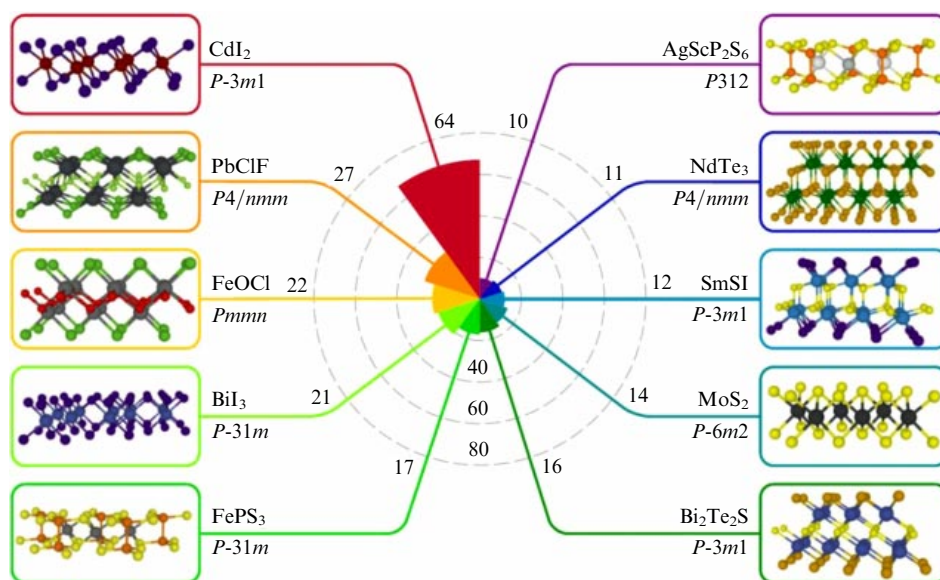


Figure 2. Polar histogram representing the number of structures belonging to the ten most frequently encountered 2D polytypes among the revealed variety of 1036 weakly bound 2D compounds. An example of atomic structure for every type and the corresponding structural formula and space group are indicated additionally [16].

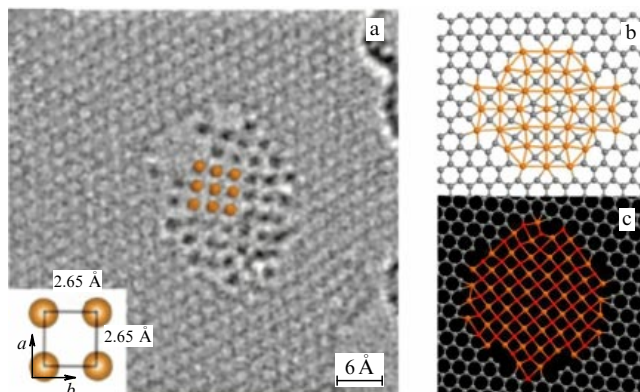


Figure 4. (a) TEM image of a two-dimensional iron-based structure in a graphene pore [25] and its interpretation as a possible compound of iron atoms with (b) carbon [26] or (c) oxygen [27].

ing these structures is due to the formation of strong directional chemical bonds in the film. However, the solution to the nontrivial problem of forming a film purely of metal atoms seems particularly promising. Indeed, due to the collectivization of electrons, metal atoms tend to form three-dimensional densely packed structures. That is why it is difficult (or even impossible) to stabilize individual free 2D metallic structures. On the other hand, such films can be obtained on surfaces or in other two-dimensional materials.

The possibility of forming a 2D layer from metal atoms was first reported in Ref. [25] describing the experimental observation of 2D Fe with an unusual square lattice inside a graphene pore (Fig. 4a). This paper demonstrated the prospects of using perforated graphene as a matrix for synthesizing two-dimensional membranes.

Interest in the presented results is due not only to the unusual structure of the obtained film, but also to its potential properties. For example, it was theoretically predicted that a 2D monolayer of Fe will possess a magnetic moment of $\sim 2.6\text{--}2.7 \mu_B$ (μ_B being the Bohr magneton), which is considerably higher than in a bulk crystal ($2.2 \mu_B$) [28, 29]. In addition, a 2D Fe film should possess a high transverse anisotropy, which can be extremely useful for applications in magnetic data recording [25]. It is also expected that 2D metals could be used to create new active catalysts and gas sensors [30] thanks to their high chemical activity, considerably different from that in bulk crystals. There are hypotheses that such systems can be superconductive [31].

The results of Ref. [25] were discussed later in many studies. Thus, the authors of theoretical papers [26, 29, 32, 33] showed that for 2D iron a densely packed hexagonal lattice rather than a square one is the most energetically favorable. This is confirmed by data from [34], where exactly this structure of 2D Fe was observed.

Because of the present disagreement between experimental and theoretical data, a number of authors [26, 27, 33] supposed that the synthesized film was a compound of iron with other atoms. Indeed, if the impurity level in experiment [25] is below the sensitivity of the electron energy loss spectroscopy (EELS) method used, then it is not possible to rule out the formation of iron compounds with carbon or oxygen rather than only a pure metal film in the experiment. In this case, the C or O atoms stabilize the square lattice of iron and allow the formation of a two-dimensional layer (see Sections 3.2 and 3.3 below). Moreover, the atomic structures

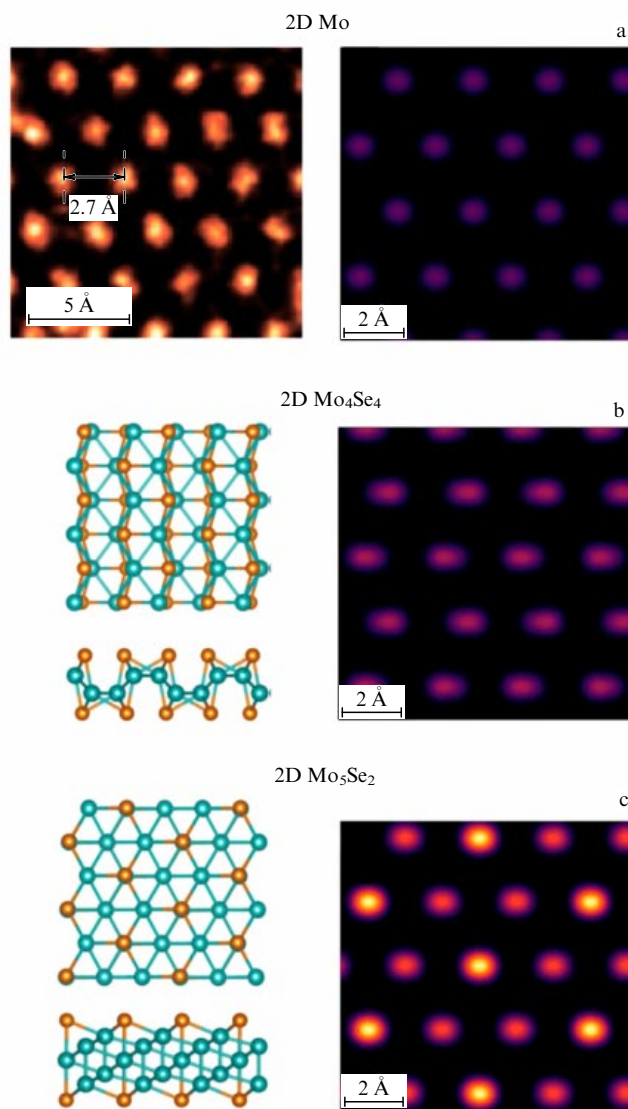


Figure 5. Comparison of an experimental image with possible models. (a) Experimental [35] and modeled STEM images of 2D Mo; (b, c) low-energy Mo₄Se₄ (b) and Mo₅Se₂ (c) structures and the corresponding modeled STEM images [37].

of FeC (Fig. 4b) and FeO (Fig. 4c) agree well with the experimental results (Fig. 4a). Thus, the length of the Fe–Fe bond in the predicted compounds FeC (2.45–2.85 Å) and FeO (2.76–2.80 Å) are closer to the experimental value (2.65 Å) than that in the ‘pure iron’ model (2.35 Å) [25].

In Ref. [35], an attempt was made to form a molybdenum monolayer from 2D MoSe₂ by exposure to a beam of electrons. The synthesized membranes had a hexagonal structure (Fig. 5a), but the experimentally measured bond lengths did not agree with theoretical predictions. In addition, the process of selenium atom removal took a long time (a few minutes), which gave rise to a question as to why other phases with intermediate stoichiometry were not observed, in contrast to, e.g., tin dichalcogenides [36].

In a subsequent paper [37], it was noted that, from experimental annular dark-field images of scanning transmission electron microscopy (STEM), it is seen that a large number of bonds have lengths of the order of 3 Å, exceeding the values of Ref. [35] (2.7 Å) by more than 10%. A similar conclusion follows from an analysis of an ideal interface

between MoSe₂ and the new phase, which implies close values of the lattice parameters of both phases. Such a large tensile strain (especially with the experimentally observed migration of Mo atoms in the membrane region taken into account) allows doubting that the hexagonal lattice is preferable. Thus, it was shown in [37] that, in contrast to 2D Fe [26, 29, 32, 33], in 2D Mo exactly the square lattice is energetically favorable. It was supposed that in experiment [35] observed was molybdenum monoselenide, MoSe, or a number of other Mo_xSe_y compounds having symmetry and lattice parameters close to those observed in the experiment, e.g., Mo₄Se₄ (Fig. 5b) or Mo₅Se₂ (Fig. 5c). It was also noted that such structures are also energetically favorable for other compositions: Mo_xS_y, W_xS_y, W_xSe_y, Mo_xTe_y, W_xTe_y.

In Ref. [38], the atomic structure of silver was studied *ab initio*, and its stability up to the melting point $T_m = 1235.08$ K was estimated. The dynamic and temperature stability was also theoretically estimated for the cases of an infinite gold monolayer [39] and a gold monolayer in a perforated graphene [40] (Fig. 6a). It was shown that in both cases at temperatures up to 1400 K the monolayer retains a regular hexagonal structure, whereas an increase in temperature leads to a transition of the compound to a liquid two-dimensional state. In this case, a fairly high longitudinal mechanical stiffness is reported for the 2D Au: $C_{11} = 52.9$ GPa, $C_{12} = 30.6$ GPa, and $C_{44} = 11.1$ GPa, which is higher than in 2D Ag and comparable to that of silicene [39]. Reference [41] additionally noted that individual atoms of gold easily diffuse over the graphene surface and join the pore edges without an energy barrier.

Experimental studies on forming 2D gold films are worth particular attention. Thus, the authors of Ref. [42] implemented a controlled destruction of the Ag–Au alloy. Under the action of an electron beam, the sample gradually became thinner with the formation of a six-coordinated monolayer structure, predicted earlier [39]. The authors of [42] explain the mechanism of monolayer formation as follows: when under exposure to an electron beam, the sample region becomes two-layer, and the coordination number of gold atoms in it reduces to six. A planar six-coordinated monolayer structure also has a coordination number of six, but possesses a higher symmetry, which makes it more energetically favorable. The atoms from the lower layer move to the upper layer, forming a nucleus of monolayer. This leads to the monolayer lattice extension and kicking the atoms from the interface or their diffusion to the surrounding alloy. As a result of the process described, a gold monolayer with an area of up to 57 nm² is formed. The atomic thickness of the film was confirmed by STEM annular dark-field imaging at large angles (Fig. 6b), an analysis of the extended X-ray absorption fine structure (EXAFS), and high-resolution transmission electron microscopy (HR TEM) with aberration correction (Fig. 6c).

The prospect of forming metallic monolayers in a matrix of another two-dimensional material offers fundamentally new possibilities for synthesizing 2D heterostructures. Thus, in theoretical paper [43], a systematic study of metal monolayers in graphene pores was carried out. As criteria for the stability of such two-dimensional films, the authors considered the energies of 2D and 3D clusters, the strength of binding metal atoms to the graphene edge, the mechanical stress at the interface due to the difference between the lattice parameters of graphene and a 2D metal, the tendency of the metal to form carbide (which makes the metal/graphene

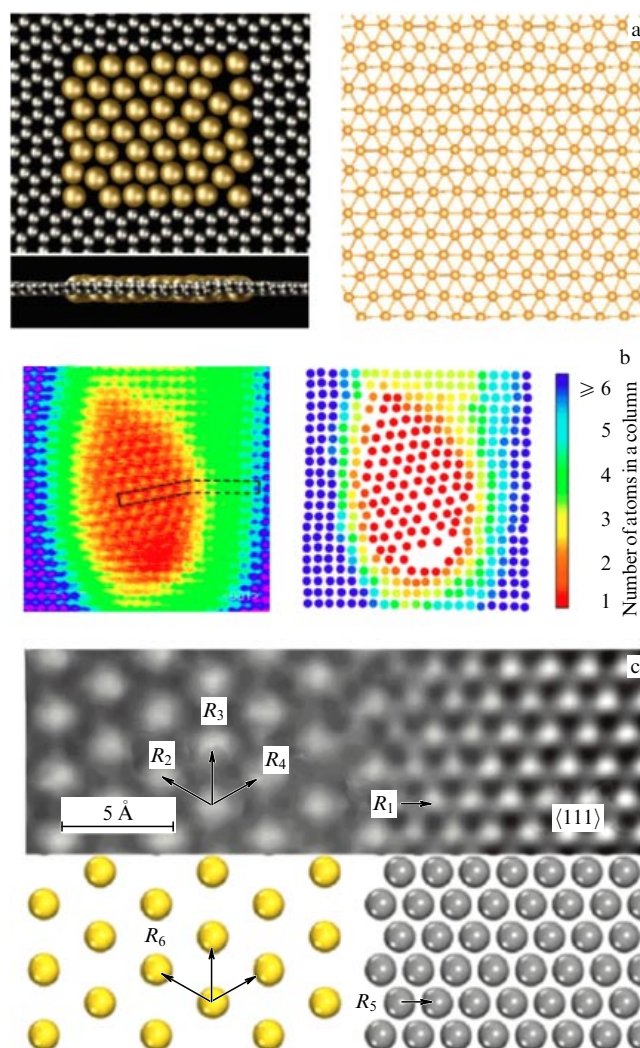


Figure 6. Gold monolayer: theoretical and experimental data. (a) The predicted structure of 2D Au in a graphene pore [40] and in the free-standing state [39]; (b, c) images of a gold monolayer obtained using STEM annular dark-field imaging at large angles (b), HR TEM with aberration correction (c), and theoretical models corresponding to them [42].

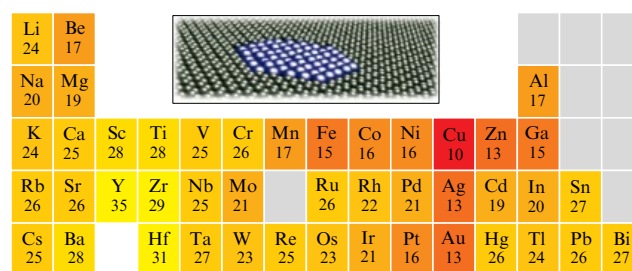


Figure 7. Balanced ranking of metals from the point of view of forming 2D structures in a graphene pore (the smaller the rank, the more likely the formation) [43].

interface unstable), and the bending modulus magnitude (i.e., the 2D metal's ability to maintain a flat structure). The resulting table, presenting the balanced ranking of metals from the point of view of forming 2D structures in graphene, is shown in Fig. 7. The atoms of Cu, Zn, Ag, and Au are marked as the most promising candidates for filling graphene pores.

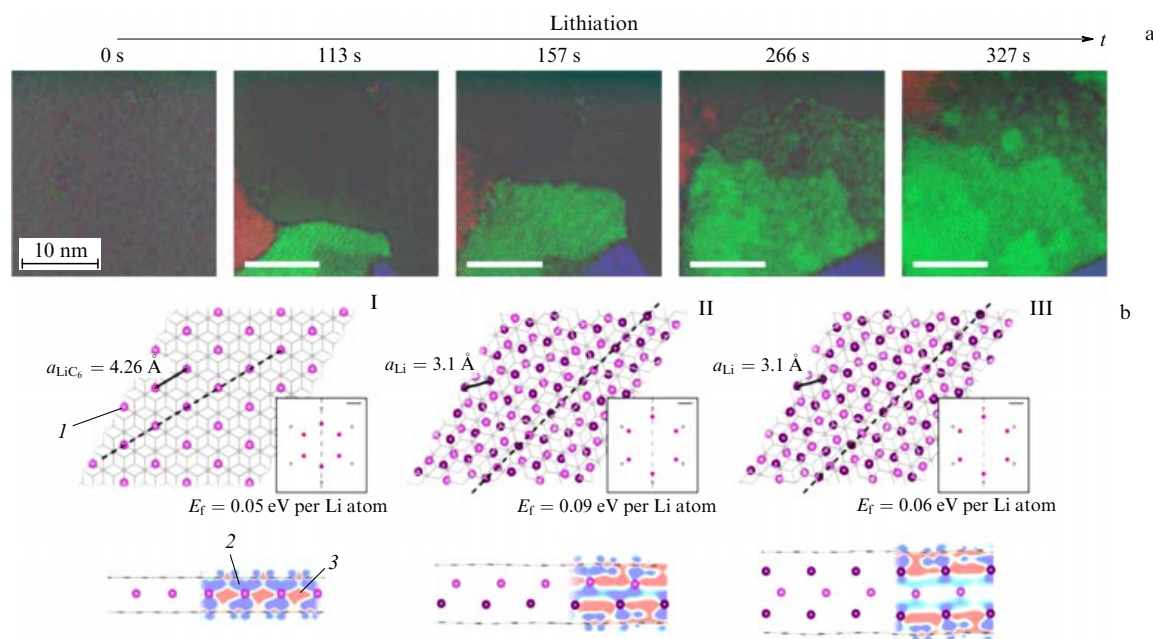


Figure 8. (Color online.) (a) Growth of 2D Li between two layers of graphene. The crystal grains of different in-plane orientations are shown in red, green, and blue, (b) 2D Li models between graphene layers, (I) monolayer C_6LiC_6 configuration with the arrangement of Li atoms in a superlattice ($\sqrt{3} \times \sqrt{3}$), (II, III) optimized two-layer (II) and three-layer (III) Li crystal. The atoms of carbon and the bond between them are shown in grey, the Li atoms in violet (I). The insets in (I–III) present diffraction patterns of the corresponding crystal structure. The contour plots in the figures represent the charge transfer between Li and graphene in comparison with separate crystals of graphene and Li. The increase in electron density (negative charge) is shown in blue (2) and the decrease in electron density (positive charge) in red (3) color [46].

While the presence of pores in graphene allows the formation of individual clusters of 2D metals, multilayer stable two-dimensional structures offer a possibility of forming a two-dimensional metallic lattice between its layers, restricting the displacement of atoms from the plane. Such a ‘nanoreactor’ was earlier successfully applied to synthesize two-dimensional ice both between graphene layers [20] and between a graphene layer and an MoS_2 one [44]. The prospect of using the graphene/ MoS_2 heterostructure was also demonstrated theoretically in [45] for the formation of two-dimensional lithium and gold. It was found that, although both metals form an atomically thin film, their atoms differently interact both with each other and with the surrounding two-dimensional matrix. Thus, Au forms a linked monolayer structure that weakly interacts with graphene and MoS_2 and retains the electronic properties of a single layer of 2D Au.

On the other hand, the Li intercalation enhances the binding with graphene and MoS_2 due to the charge transfer to the layers. In this case, the repulsion between Li atoms allows a hypothesis that the monolayer can be formed only by application of external forces. This was implemented in Ref. [46], where the authors managed to realize controllable processes of lithiation (delithiation) of a graphene bilayer by applying a voltage of $U_G = 5$ V ($U_G = 0$ V). The intercalated Li rapidly diffused in the plane and uniformly distributed over the entire graphene bilayer, forming a two-dimensional film (Fig. 8a).

The optimization of the monolayer lithium phase geometry has shown that the C_6LiC_6 configuration with Li located in a commensurate ($\sqrt{3} \times \sqrt{3}$) supercell with a lattice constant of 4.26 Å is energetically preferable (Fig. 8bI); however, two- and three-layer structures are close in energy. An analysis of electronic structure and charge distribution revealed considerably less charge transfer from Li to

graphene for multilayered structures than the C_6LiC_6 phase. A general tendency towards a decrease in the mean charge transfer upon increasing the number of Li layers was also revealed. A possible explanation is that some of the electrons participate in the formation of a bond between positively charged Li ions in multilayer Li systems, rather than being transferred to the electronic states of graphene. This is seen, e.g., from a comparison of charge density distribution with that in isolated graphene crystals and Li (insets in Fig. 8b).

It was predicted that a stable lithium monolayer could be implemented for the case of AA stacking of graphene [46]. Since such a stacking is energetically unfavorable, it is possible to use bigraphene forming moiré pattern. In that case, Li atoms tend to form 2D clusters in the regions of AA-stacking and find themselves at the centers of carbon hexagons [47].

Besides Li, Ref. [48] considered other alkali metals, namely, Na, K, Rb, and Cs. It was shown that monolayer structures of K, Rb, Cs could be stabilized between the layers of AA-stacked graphene. They are also the most energetically favorable of all the considered metals when forming a monolayer between the layers of MoS_2 .

Two-dimensional metallic layers of copper can be formed between layers of other metal dichalcogenides (NbS_2 , $NbSe_2$, TiS_2 , TaS_2 , and VS_2) at room temperature and atmospheric pressure, as was experimentally demonstrated in Ref. [49].

The presented results are particularly topical in view of studies of two-dimensional heterostructures, in which monolayers of different compositions are combined into a new nanomaterial with controllable properties [50]. The synthesis of metal monolayers on different nanostructures can allow the injection of spins into 2D structures that can be a base for spintronic devices [51].

It is theoretically shown in [52] that graphene is able to stabilize a monolayer of rhodium atoms. In the resulting two-layer film, the Rh atoms have a discrete set of magnetic moment values of $0 \mu_B$, $0.45 \mu_B$, and $0.81 \mu_B$, which is due to film corrugation. The authors conclude that the predicted effect of transverse magnetic anisotropy in the Rh/graphene bilayer can be used for spin transportation of polarized charge carriers in an Rh layer.

Metallic monolayers are also promising for use as catalyzers, as was proposed, e.g., for a platinum monolayer [30, 53] and palladium [30] on graphene.

3. Monolayer films of metal compounds

As mentioned in Section 2, many studies of two-dimensional metallic films stimulate intense discussion, since there are often reasons to suspect that a compound rather than a pure metallic film is obtained in experiments. In this sense, directed covalent and ionic bonds are more suitable for the role of a basic type of interatomic bond to form stable 2D layers.

In this section, we proceed to theoretical and experimental studies of monolayer films consisting of compounds of metal atoms with atoms of carbon, oxygen, etc.

3.1 Ionic graphitization effect

To date, there have been many methods to synthesize various nanomaterials, differing in homogeneity of composition and properties [54]. For example, well known are the methods of chemical vapor deposition (CVD), magnetron sputtering, or synthesis in nanoreactors, which are bottom-up techniques. At the same time, two-dimensional nanostructures up to atomically thin ones can be directly produced from bulk materials using sonochemistry, electrical explosion, mechanical exfoliation (e.g., of graphene), i.e., methods united by the top-down paradigm. However, in addition to these methods of nanomaterial synthesis, there are a number of internal physicochemical mechanisms that produce new compounds. Among these, the process of graphitization of carbon materials merits particular attention, as does its 'noncarbon' counterpart.

A tendency toward graphitization of diamond surfaces is well known. It plays a dominant role in the case of superthin diamond films of nanometer thickness, diamanes [55]. Indeed,

graphitization leads to the spitting of the diamond films into separate monolayers of graphite, making their structure unstable [56, 57]. It is interesting that the effect of splitting of superthin films also takes place in the case of other compositions with ionic-covalent interatomic interaction, the nature of splitting being fundamentally different. This effect, which we called 'ionic graphitization' in [58], was initially predicted for the case of films with a polar surface having the wurtzite structure [59, 60] and later extended over the family of films with the zinc blende and rock salt structure [58, 61–64].

The effect is seen from a direct comparison of bonding energies for films with a polar surface and for corresponding graphite-like structures [62] (Fig. 9a). From the dependence of the energy difference on the number of layers in the film, one can see its crossing for BP, SiC, and NaCl at the number of layers 3, 4, and 11, which evidences the energetic preference of graphite-like film with a small number of layers. Such a comparison is convenient also because it shows the impossibility of splitting silicon films into graphite-like layers, as well as the tendency to graphitization of superthin diamond films.

In this case, it is important to note that the fundamental reason for such splitting is different for ionic and covalent materials. Thus, the redistribution of electron density in the case of covalent materials is restricted to the surface and falls to zero in a bulk material (Fig. 10a). In materials with an ionic contribution (Fig. 10b,c), due to the presence of polar surfaces, the redistribution of electron density is much stronger and involves a greater number of layers, which gives rise to a dipole moment directed perpendicular to the surface. The resulting surface stresses split the film into separate layers, removing the dipole moment and decreasing the surface contribution to the total energy of the system. It is important to note that the energy of a graphite-like film for several layers is often even lower than that of a film not only with a polar surface but also with a nonpolar one, as observed, e.g., in GaN (Fig. 9b).

The key contribution of the electric dipole moment was demonstrated by the example of the NaCl compound in [63]. It was shown that the dependence of the magnitude of the dipole moment directed perpendicular to the (111) surface on the thickness of a graphite-like and cubic film correlates with the energy difference between these structures (Fig. 10d). In this case, the energy of interlayer coupling in graphite-like

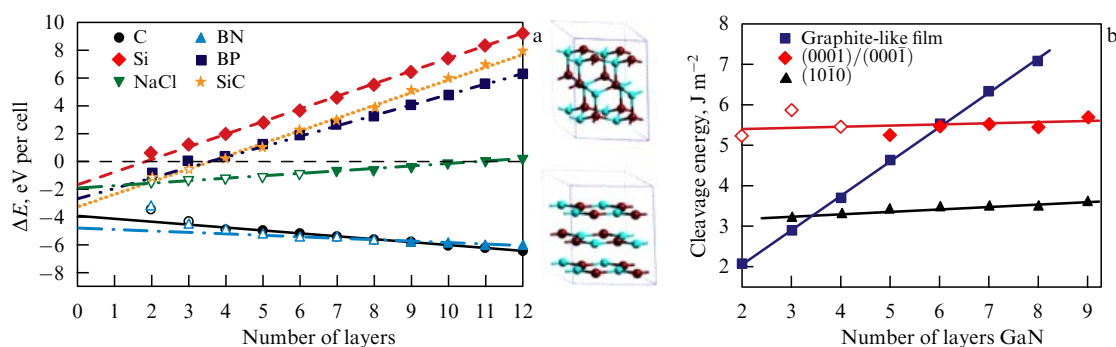


Figure 9. Ionic graphitization effect, i.e., the splitting of thin films with a polar surface; (a) the difference in binding energy between a film with a polar surface having the structure of zinc blende or rock salt and a graphite-like structure, depending on the number of layers for the case of sodium chloride, boron nitride, boron phosphate, and silicon carbide [62]. For comparison, the data for carbon and silicon are presented. A positive value indicates the cubic lattice preference, a negative one means that the graphite-like structure is preferable; (b) on the left — the atomic structure of a three-layer film with a wurtzite structure having the polar surface (0001)/(0001) and the corresponding split graphite-like film; on the right — a comparison of film cleavage energy for gallium nitride film with a wurtzite structure having a polar and a nonpolar surface, and a graphite-like film, depending on the number of layers [60].

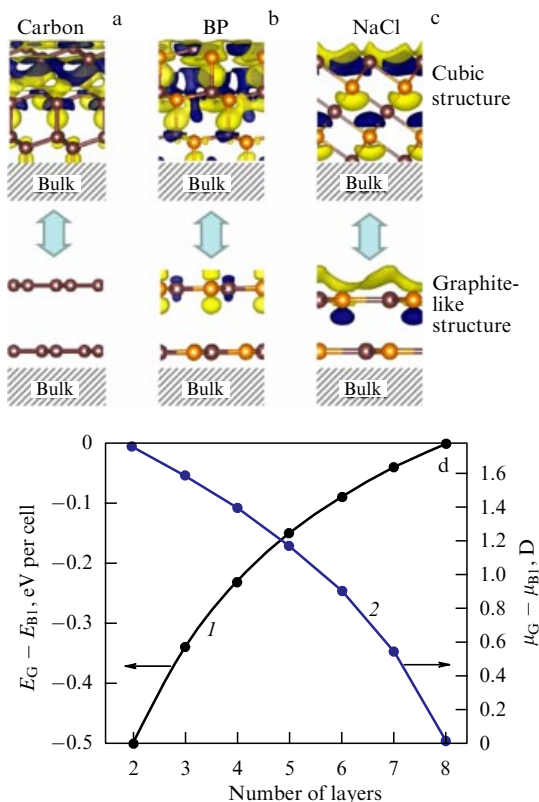


Figure 10. (Color online.) Difference in electron density $\Delta\rho$ between the surface and the corresponding crystal with cubic (surface (111)) and graphite-like (surface (0001)) structures for the cases of (a) carbon, (b) boron phosphate, and (c) sodium chloride. The isosurface value $\Delta\rho_{\pm} = \pm 5 \times 10^{-4} e \text{ \AA}^{-3}$. The areas with electron excess are shown dark, the areas with electron deficiency are light [62]. (d) The energy difference per stoichiometric unit (black line 1) and the difference between dipole moments (blue line 2) for graphite-like and cubic film of NaCl depending on the number of layers (thickness) [63].

films of ionic compounds corresponds by order of magnitude to the van der Waals binding energy and is comparable to the appropriate value for a graphite crystal [63]. This evidences the relative independence of individual layers in the film and the possibility of their separation by various exfoliation techniques using liquid solutions [65] or mechanical actions [1]. The existence of graphite-like NaCl on a diamond surface (110) was predicted using evolution algorithms. It was shown that due to strong bonding with the substrate the grown two-dimensional material inherits the substrate symmetry. The predictions were confirmed experimentally using the magnetron sputtering method. By electron diffraction, the formation of a thin layer of graphite-like NaCl on the surface of a polycrystalline and monocrystalline diamond was fixed [66].

Thus, it is predicted that in films of various compositions as thick as a few atomic layers the formation of new graphite-like phases is possible. This enlarges the variety of phases in materials with prevailing ionic interatomic bonds.

The theoretical conclusions were confirmed in a number of experimental studies of silicon carbide [67], aluminum nitride [68], and zinc oxide [69]. The authors of [68] managed to obtain triangle g-AlN clusters up to 12 monolayers thick, which fully agrees with the prediction [60], in which the energetic preference of g-AlN film over w-AlN film was observed with the same number of layers. In the subsequent paper [70], even thinner films of graphite-like aluminum

nitride up to 5–6 monolayers thick were obtained on the Si(111) surface.

3.2 2D monoxides of transition metals

The theoretically predicted possibility of forming two-dimensional layers from initially nonlayered materials, such as cubic [62] and wurtzite [60] ion-covalent crystals, considerably extends the potential family of two-dimensional materials. These predictions also apply to metal oxides. Thus, in Ref. [64], it was shown that for MgO, both in the freestanding state and upon deposition on an Ag(111) substrate, a transition from the rock salt structure to the hexagonal phase is possible, when the film thickness is below a critical value.

In a series of experimental and theoretical studies [59, 69, 71–73], the transformation of ZnO from the wurtzite phase into the two-dimensional stable graphite-like g-ZnO structure (Fig. 11a) was confirmed. As zinc oxide (ZnO) is in the class of II–VI semiconductors, under standard conditions it possesses the wurtzite structure and is a key technological material. Its noncentrosymmetric crystallographic phase exhibits strong piezoelectric and pyroelectric properties. For these reasons, ZnO is frequently used in the production of such devices as mechanical drives and piezoelectric sensors. In addition, ZnO is an n-type semiconductor with a wide bandgap (3.37 eV) and high binding energy of excitons (60 meV), which makes it an attractive material for short-wave optoelectronic applications and ultraviolet (UV) luminescence at room temperature [74]. At the same time, ZnO is transparent to visible light. The wurtzite ZnO is a base for an entire family of nanostructures, such as nanotubes, nanowires, nanorods, nanoribbons, and tetrapods [74, 75].

In recent paper [72], two-dimensional zinc oxide clusters with a hexagonal structure in graphene pores were discovered using TEM methods. This result additionally confirms the prospectiveness of using graphene as a matrix for growing new two-dimensional materials. In this case, the formation of bonds with the boundaries of nanopores facilitates g-ZnO stability, but restricts its transverse size.

The experimental detection of g-ZnO films with the number of atomic layers as small as four [69, 73, 77–79] fully corresponds to the theoretical estimate from above, proposed in Ref. [60]. In this paper, it was shown that graphite-like films of ZnO are energetically more preferable than the wurtzite phase, with the nonpolar and polar surfaces having thicknesses up to five and nine layers, respectively.

In the most widely used method of synthesis of g-ZnO layers, the process of chemical vapor deposition on a metallic substrate under superhigh vacuum conditions is used (Fig. 11b). In such a process, metallic Zn is deposited on a metallic substrate and oxidized either in the process of reactive evaporation or after the deposition of Zn (post-oxidation), forming layers of g-ZnO. Various metals that possess a (111) surface, e.g., Pd [80], Pt [81], Au [73, 78], Ag [69, 77, 79], can be used as a substrate for growing.

In Ref. [76], the soft hydrothermal method was used to synthesize g-ZnO. An aqueous solution of zinc nitrate hexahydrate ($\text{Zn}(\text{NO}_3)_2 \cdot 6\text{H}_2\text{O}$), hexamethylenetetramine, and sodium citrate ($\text{Na}_3\text{C}_6\text{H}_5\text{O}_7$) was placed in a Teflon container and pressurized in an autoclave. After heating for 3 hours at a temperature of 95°C, it was filtered and dried. The TEM image in Fig. 11c shows the synthesized nanoparticles of crystalline ZnO, evidencing the presence of single-layer and two-layer g-ZnO films.

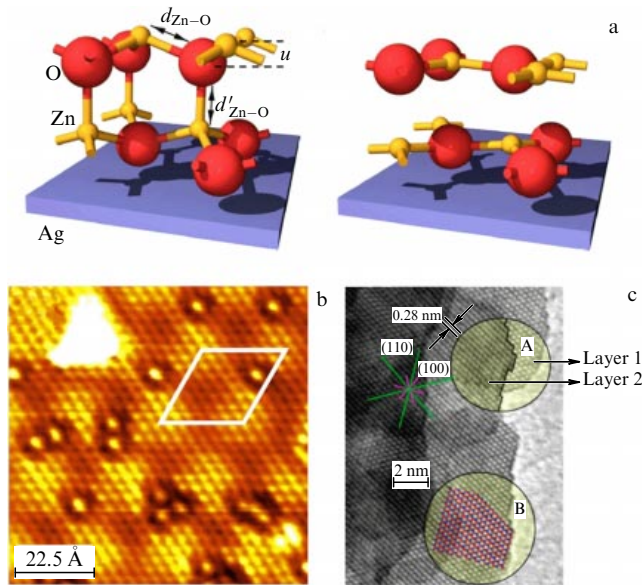


Figure 11. (a) Schematic model of ZnO in the wurtzite phase and in the form of graphite-like monolayers, detected experimentally; (b) STM image of two-layer graphite-like ZnO of an Ag(111) substrate [69]; (c) TEM image of ZnO monolayers in the regions A and B, obtained by the hydrothermal method [76].

In a number of theoretical papers, the electronic, magnetic [82–84], elastic, and piezoelectric properties [85, 86] of g-ZnO monolayers were studied. According to estimates, the bandgap in g-ZnO amounts to 3.58–5.64 eV [82, 86], which is greater than in the wurtzite phase. The values of the parameters that characterize the mechanical properties of g-ZnO were determined. Without taking into account the indefinite monolayer thickness, the elastic constants and piezoelectric modules in g-ZnO have the following values: $C_{11} = 131 \text{ N m}^{-1}$ [85], 102 N m^{-1} [86], 92.6 N m^{-1} [87], 86 N m^{-1} [88], $C_{12} = 43 \text{ N m}^{-1}$ [85], 72 N m^{-1} [86], 61.9 N m^{-1} [87], 57.3 N m^{-1} [88] (which is less than in graphene, where $C_{11} = 358.1 \text{ N m}^{-1}$, $C_{12} = 60.4 \text{ N m}^{-1}$ [89]), $e_{11} = 0.48 \text{ e Å}^{-1}$ [85], 0.18 e Å^{-1} [86], 0.17 e Å^{-1} [87]. The latter values can be compared with the data for h-BN (0.23 e Å^{-1} , 0.16 e Å^{-1} [90], 0.15 e Å^{-1} [91]). In this case, the bending stiffness of a monolayer amounts to 0.15 eV [85], which is an order of magnitude less than for graphene (1.46 eV [92]), and the Poisson coefficient $\nu = C_{12}/C_{11}$ (0.71 [86], 0.67 [87, 88]) is more than three times higher than for graphene (0.17 [89]). Note that the results of [85] considerably differ from all subsequent studies.

In theoretical papers [93–95], vertical heterostructures based on graphene and g-ZnO were also investigated. Hu et al. [93] reported weak van der Waals interaction and, therefore, a virtually complete absence of charge transfer between graphene and the g-ZnO monolayer, as well as the preservation of graphene properties near the Fermi level. In particular, the Fermi velocity at the Dirac point of graphene in the heterostructure considered almost coincides with that in isolated graphene. The authors also predicted the growth of efficiency of UV absorption in the graphene/g-ZnO heterostructure, which can find application in photocatalysis and photovoltaics. In another paper by Yao et al. [94], in addition to an ideal graphene/g-ZnO heterostructure, oxygen vacancies were also studied, and it was shown that their presence does not affect graphene's electronic properties. As in [93], the

authors concluded that g-ZnO can be considered a prospective substrate for graphene.

The graphene/MoS₂/g-ZnO/graphene heterostructure was studied in Ref. [95]. It was shown that the presence of a strong interaction between edge graphene layers and MoS₂/g-ZnO leads to the formation of a direct bandgap, in contrast to the case of an isolated MoS₂/g-ZnO bilayer. The change in orientation of graphene sheets with respect to MoS₂ and ZnO leads to splitting of the graphene energy bands because of different degrees of graphene doping. Calculations of electronic properties have also shown a high doping of graphene layers and zero bandgap, which allowed concluding that there is a possibility of using such structures in photoelectric and valitronic applications.

It is worth noting that a stable two-dimensional phase can be obtained not only by splitting an initially bulk compound. Moreover, the two-dimensional structure can exist in the absence of its bulk analog as well. Thus, for example, the cubic phase of CuO is unstable in a free state. However, Kano et al. [96] and Yin et al. [97] for the first time experimentally observed two-dimensional copper oxide on a graphene substrate. Nevertheless, in contrast, for example, to the g-ZnO monolayer, the 2D CuO lattice appeared to be rectangular (Fig. 12a) rather than hexagonal (graphene-like). Subsequent density functional theory (DFT) calculations confirmed that only the copper monoxide clusters can retain a two-dimensional lattice on graphene, in contrast to copper carbide or copper film.

Quantum-chemical calculations confirmed that oxygen atoms tend to occupy the center of the square of copper atoms, thus strengthening the lattice and reducing the out-of-plane distortion. The position of oxygen atoms in 2D copper oxide is also confirmed by a STEM analysis. Figure 12b presents the experimental and simulated STEM images, and the intensities of linear profiles in Fig. 12d correspond to the white dashed line. The proximity of experimental and theoretical profiles allows a conclusion that two observed periodically repeated peaks with different intensities are formed exactly by Cu and O atoms. In Ref. [97], it was also predicted that two-dimensional copper oxide is a semiconductor with a bandgap width of 2.7 eV and weak antiferromagnetic ordering, whereas the corresponding bulk crystal is paramagnetic with a bandgap of the order of 1.4–1.7 eV [98].

The authors of Ref. [99] investigated the 2D CuO in a pore of two-layered graphene. Besides the study of specific feature stabilization of CuO clusters in a bigraphene pore, the possibility of 2D Cu hexagonal metallic lattice formation was predicted. The formation of spin-polarized states at the interface between CuO and graphene was revealed.

Another theoretical paper [27], devoted to two-dimensional iron oxide, also considered the exfoliation process of a bulk FeO crystal into separate monolayers according to the abovementioned mechanism of ionic graphitization of crystals having a rock salt structure. The authors showed that when the thickness of the initial film of the bulk FeO crystal is less than 9 layers, the existing dipole moment tends to separate it into individual monolayers of single-atom thickness, as follows from the energy balance presented in Fig. 13a. In contrast to earlier studied two-dimensional salts [58], in this case the energetically preferable atomic structure of 2D FeO is a planar rectangular lattice ($a = 2.80 \text{ Å}$, $b = 2.76 \text{ Å}$, Fig. 13b) similar to earlier obtained two-dimensional copper oxide [96], rather than a hexagonal lattice. The 2D FeO was shown to be a semiconductor with a bandgap of 2.12 eV

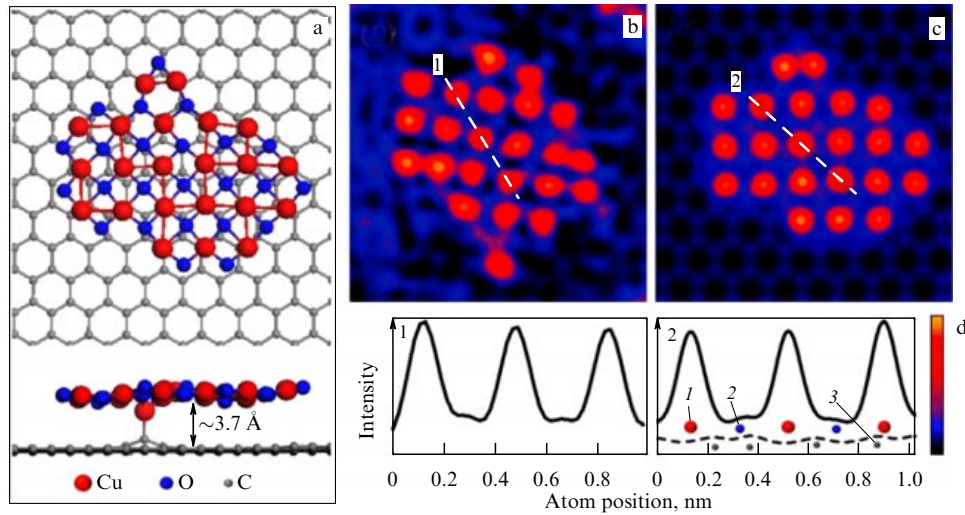


Figure 12. (Color online.) Comparison of experimental and simulated data for 2D copper oxide. (a) Atomic model of a cluster of 2D copper oxide on graphene, top and side view, after optimization by DFT method. (b) Magnified and filtered STEM image of a 2D CuO cluster. (c) Simulated STEM image for model (a). (d) Linear profiles corresponding to the dashed lines in Figs (b) and (c). Atoms of Cu, O, and C and their positions on the profile are denoted by red (1), blue (2), and grey (3) balls, respectively. The dashed profile line in (d) shows the intensity of a separately simulated graphene sheet without the cluster of 2D copper oxide [96].

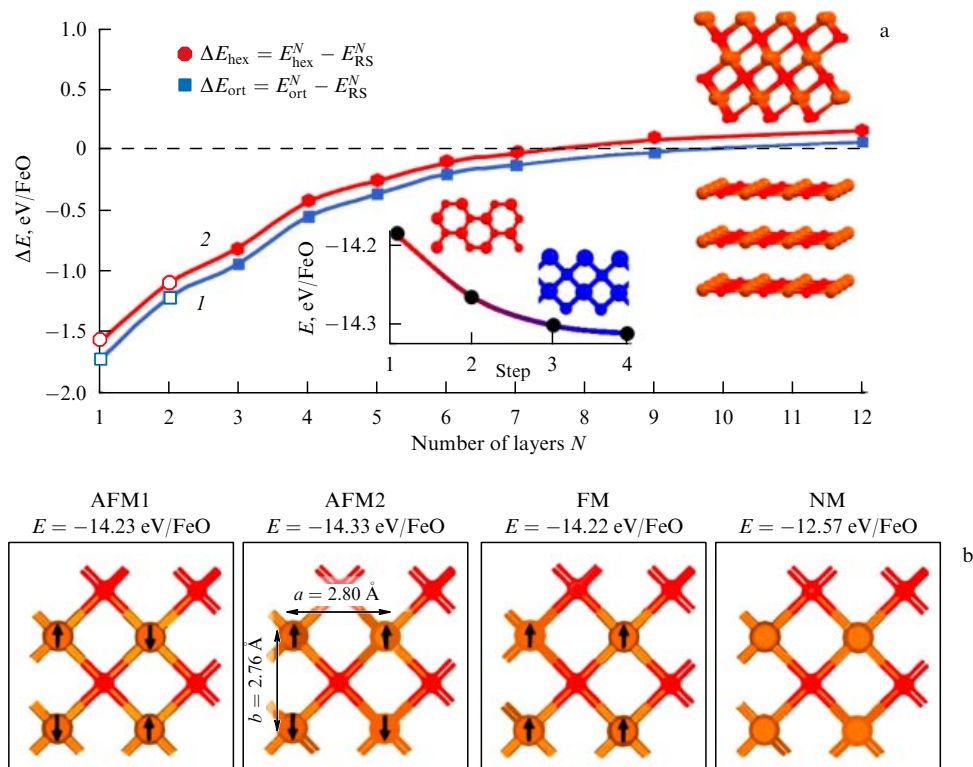


Figure 13. (Color online.) (a) Energy difference between N monolayers of 2D FeO (AA stacking) with a two-dimensional rectangular (E_{ort}) or hexagonal (E_{hex}) lattice and an N -layer film of FeO(111) in the rock salt phase (E_{RS}), shown by blue (1) and red (2) markers, respectively. The inset shows the barrier-free transition of the hexagonal lattice into the rectangular one. (b) Magnetic configurations of a 2D FeO monolayer, where AFM1 and AFM2 are antiferromagnetic, FM are ferromagnetic, and NM are nonmagnetic configurations. For the energetically favorable AFM2 configuration, the lattice parameters are presented [27].

(2.05 eV for a bulk crystal) and to possess antiferromagnetic ordering. The difference in energy between the antiferromagnetic and nonmagnetic state equals 1.7 eV/FeO for the case of 2D FeO and 1.5 eV/FeO for the case of a bulk crystal. The presented values substantially exceed those for 2D copper oxide [96]. Nevertheless, the calculation of phonon frequencies and flexural rigidity demonstrated the instability of a free

monolayer. To analyze the possibility of stabilizing 2D FeO, planar heterostructures based on iron oxide and graphene were considered. The authors of [27] derived analytical expressions for the energy of the 2D FeO/graphene interface under the arbitrary relative orientation of the heterostructure components and described the equilibrium form of a two-dimensional iron oxide cluster in a graphene pore depending

as a result of pseudo-Jahn-Teller distortion, which leads, on the one hand, to an increase in stability of σ -bonds and, on the other hand, to destabilization of π -bonds. However, since the first effect prevails over the second one, the total stability of the structure increases [109]. The length of an Si–Si bond in the corrugated state (2.247 Å) is greater than in the planar structure (2.226 Å), which leads to a larger unit cell size [107, 109]. Nevertheless, in the corrugated structure, the electrons are more delocalized and possess a lower energy of electron–electron repulsion.

The out-of-plane displacement of atoms also causes partial sp^3 hybridization of bonds in silicene and germanene, which essentially distinguishes their structure from that of graphene. Hence, in contrast to the crystals of silicon and germanium, of which only sp^3 hybridization is characteristic, in the cases of 2D Si and 2D Ge the mixing of sp^2 and sp^3 states takes place. This leads to a decrease in structure stability due to the appearance of unsaturated bonds, but, on the other hand, the corrugation is an additional degree of freedom, which can be used to modify the material properties, for instance, to open a bandgap in their electronic structure.

4.1.1 Silicene synthesis. Because of the absence of a graphite-like phase of silicon in nature, silicene and other such materials can be synthesized in the framework of the bottom-up approach, e.g., by epitaxial growth on a substrate.

This process occurs via the condensation and self-organization of thermally evaporated silicon atoms on a substrate. Although silicene can be synthesized on various substrates (Ir [110], MoS_2 [111], ZrC [112], Pb [113], Ru [114], and graphite [115]), silver is most frequently chosen for epitaxial growth [116–122]. Moreover, an epitaxial film of Ag(111) on substrates of mica or Si (111) [123] allows avoiding unpractical usage of expensive single-crystal silver and ensures the separation of material in subsequent processing. The frequent choice of Ag(111) as a substrate is determined by the close values of lattice parameters of silver and silicene. It is worth noting that the use of Ag(110) and Ag(100) surfaces instead of Ag(111) can lead to the appearance of silicon nanoribbons, as shown in a number of experimental and theoretical papers [124–126].

For silicene obtained on Ag(111), reconstructions of a different kind are observed, denoted in the literature in two ways: relative to a unit cell of the silicene surface or relative to Ag(111). Thus, relative to Si, the most known reconstructions are denoted as 3×3 , $\sqrt{7} \times \sqrt{7}$, and relative to Ag(111) as 4×4 , $\sqrt{13} \times \sqrt{13}$, $2\sqrt{3} \times 2\sqrt{3}$. Hereafter, for these types of

reconstructions only the notation relative to a unit cell of Ag(111) will be presented. They have the form $(n \times n)R\alpha$, where n is the silicene supercell length relative to a unit cell of the Ag(111) surface, and $R\alpha$ is the angle between the Si [110] direction and Ag [110] direction (Fig. 16). Also known is the reconstruction $\sqrt{3} \times \sqrt{3}$ or $4/\sqrt{3} \times 4/\sqrt{3}$ (relative to a unit cell of a silicene surface or Ag(111), respectively). This reconstruction is commonly denoted as $\sqrt{3} \times \sqrt{3}$, and in this review we will also follow this notation.

From a geometrical point of view, a finite number of reconstruction types can be observed on Ag(111). Indeed, all the superstructures found could be obtained by rotating the silicene layer relative to the silver surface [127]. Figure 16a schematically shows the (111) silicon layer and the distances between the centers of the lattice hexagons. Figure 16b depicts on the same scale the silver surface with sectors of different radii, equal to the distances specified in Fig. 16a.

The silicene phase $(\sqrt{4} \times \sqrt{4})R0^\circ$ or simply 4×4 has been most frequently observed in experiments [116, 117, 119, 123, 127–130]. As seen from the image in Fig. 17a, obtained by scanning tunneling microscopy (STM), this phase consists of two triangular elements, each containing three bright spots, which makes this phase very similar to the well-known 5×5 reconstruction of the silicon surface Si(111). It is remarkable that between different 4×4 domains a separate metastable phase with the 4×4 periodicity can be observed, denoted as $4 \times 4-\beta$ [131].

The phase $(\sqrt{13} \times \sqrt{13})R13.9^\circ$ [116, 119, 121, 123, 127, 128, 130, 131, 135] usually coexists with the phase 4×4 , which evidences their close thermal stability [116, 131, 135]. Such a mixed structure can completely cover the substrate surface. Depending on the annealing temperature, the ratio of areas of these two phases can significantly vary. As in the 4×4 phase, in the $\sqrt{13} \times \sqrt{13}$ phase the triangular elements were also observed, related to the out-of-plane atoms. For this phase, several theoretical models were also proposed, one of which is illustrated in Fig. 17b.

In contrast to the coexisting phases 4×4 and $(\sqrt{13} \times \sqrt{13})R13.9^\circ$, the phase $(2\sqrt{3} \times 2\sqrt{3})R30^\circ$ [116, 119, 121–123, 127, 128, 130, 136] is observed all over the Ag substrate. It can be obtained by annealing both 4×4 and $(\sqrt{13} \times \sqrt{13})R13.9^\circ$. For example, in Fig. 17b, a periodic pattern of brighter areas is clearly seen, its magnification demonstrating a structure consisting of ideally ordered hexagonal rings [137].

The phase $(\sqrt{3} \times \sqrt{3})R30^\circ$ [116, 118, 133, 138] (Fig. 17d) is rather interesting from the point of view of atomic structure and physical properties. In a unit cell, only one atom of silicon

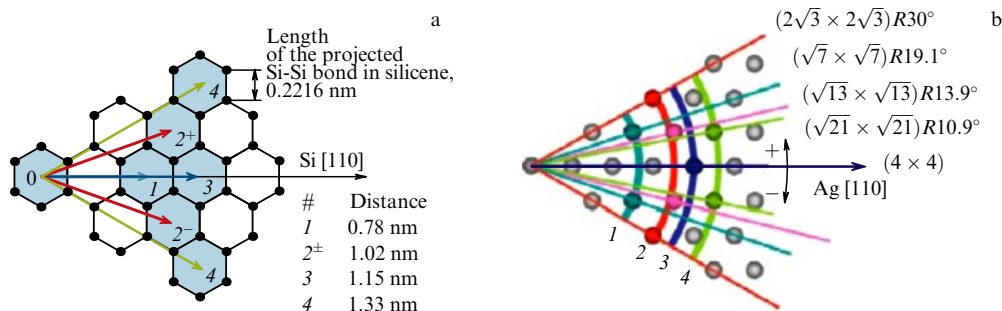


Figure 16. Diagram of all possible superlattices formed by a monolayer of silicon and the Ag(111) surface. (a) Silicon monolayer structure. The distances between the hexagon #0 and hexagons from #1 (the shortest) to #4 (the longest) are shown in the Figure. (b) Ag(111) substrate with all possible superlattices. Different sectors show possible coincidences between the hexagonal silicon layer and the Ag(111) substrate [127].

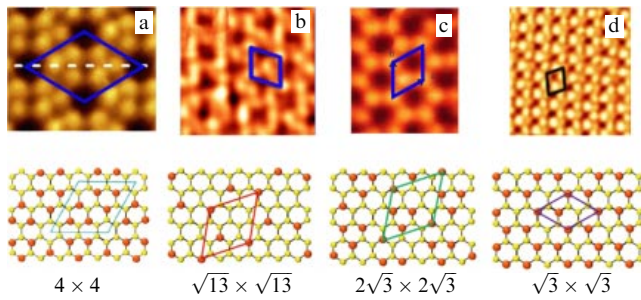


Figure 17. Epitaxial silicene growth on a substrate of Ag(111). Silicene reconstruction types: (a) 4×4 , (b) $\sqrt{13} \times \sqrt{13}$, (c) $2\sqrt{3} \times 2\sqrt{3}$, (d) $\sqrt{3} \times \sqrt{3}$. The first row shows high-resolution STM images: (a) [132], (b) [121], (c) [116], (d) [133]. The second row illustrates the proposed atomic geometry of silicene on a substrate [134].

is displaced up from the plane, whereas the remaining atoms are approximately at the same depth. To date, there is no general opinion on whether this phase is characteristic of a silicon monolayer or appears only in the case of multilayer silicene synthesis [119, 120, 132, 139, 140].

An attempt to construct a phase diagram for silicene placed on a silver substrate, depending on the substrate temperature and degree of silicon deposition, was made in a number of experimental and theoretical papers [119, 141, 142].

4.1.2 Germanene synthesis. The most reliable publication reporting germanene synthesis is the paper by Dávila et al. [143]. In this paper, germanium was deposited onto an Au(111) substrate, as a result of which a structure with the $\sqrt{3} \times \sqrt{3}$ reconstruction was formed on a gold $\sqrt{7} \times \sqrt{7}$ supercell. It was later theoretically shown in [144] that a strong interaction exists between the layer of germanene and the gold upon modification of the layer hybridization. Note that germanene with the 1×1 reconstruction was also obtained on a supercell of Au(111) of a similar size [145].

The germanene was successfully synthesized on Al(111) [146, 147] with the reconstruction 2×2 on a substrate supercell 3×3 . Data from STM, photoelectron diffraction, and *ab initio* calculations have shown [146] that the sheet of germanene is a regular corrugated structure. In Ref. [147], it was proved that the interaction between the germanene layer and the substrate is electrostatic with charge transfer from Al atoms to Ge atoms. Germanene was also successfully obtained on Cu(111) [148].

In Refs [149, 150], platinum was deposited onto a Ge(110) substrate followed by annealing up to a temperature of about 1100 K. Electron microscopy studies have shown that at temperatures exceeding 1040 K on the surface of Ge(110) eutectic droplets of $\text{Pt}_{0.22}\text{Ge}_{0.78}$ are formed. When cooled, the eutectic phase experiences spinodal decomposition into the pure Ge phase and Ge_2Pt . The excess Ge separates from the surface of solidified Ge_2Pt droplets and forms a honeycomb corrugated structure, which was interpreted as germanene with a Dirac character of electronic structure.

It was also possible to retain the electronic structure of two-dimensional germanene in the process of its synthesis on h-AIN/Ag(111) [151], MoS_2 [152], and graphite [153].

4.1.3 Electronic properties of silicene and germanene. Calculations based on the tight binding model and the density functional theory predicted that the quasiparticles in a free-

standing silicene and germanene obey a linear dispersion law near the Dirac points K and K'. This means that the quasiparticles in these materials are similar to massless relativistic particles with the dispersion law $E = \hbar v_F k$, where v_F is the Fermi velocity [108]. However, the structure corrugation and the great atomic mass of silicon and germanium in silicene and germanene, respectively, increase the spin-orbit coupling and give rise to a bandgap formation near the Dirac point (Fig. 18). Thus, the spin-orbit bandgap in silicene (~ 1.55 meV) and germanene (~ 23.9 meV) [154] is greater than in graphene (~ 0.001 meV) [155] (Fig. 18a–c). So great a bandgap width in germanene makes it an ideal candidate for observing the spin quantum Hall effect at experimentally available temperatures.

The corrugated structure of silicene and germanene determines the dependence of their electronic properties on the external conditions, which can be exploited for controlled modification of properties. For example, it was predicted that external electric and magnetic fields, mechanical strain, and temperature can create various electronic states in silicene, including semimetal, semiconductor, and dielectric phases, as well as about 16 phases of a topological insulator [158].

The possible existence of a Dirac cone in silicene was reported for the first time in experimental paper [117], where angle-resolved photoemission spectroscopy (ARPES) was used to study the 4×4 phase on an Ag(111) surface. Later, the electronic properties of silicene on Ag(111) were investigated in [157] using ARPES, diffraction of low-energy electrons, and X-ray photoemission spectroscopy, with similar results obtained. In Figure 18d, it is seen that in the ARPES spectrum the silicene bands with linear dispersion are observed crossing at ~ 0.3 eV below the Fermi level. For epitaxial silicene, v_F can be determined from Fig. 18d and has the value $v_F = 1.3 \times 10^6$ m s $^{-1}$, which is comparable with the corresponding value for graphene [159, 160].

The experimental data presented initiated intense discussion, since the linear part of the band exceeds 3 eV (greater than in graphene), and the possible interaction of silicene with the substrate can determine the presence of a small bandgap at the Fermi level [161].

It is possible to understand the nature of quasiparticles in silicene on Ag(111) from their behavior in a magnetic field directed perpendicular to the sample. Indeed, in this case, it is possible to observe clearly expressed peaks of Landau levels in the tunneling spectra. Such peaks are observed experimentally in graphene and highly oriented pyrolytic graphite (HOPG) [162], but are absent in silicene [163] (Fig. 18e). This fact means that in silicene on an Ag(111) surface Dirac two-dimensional fermions are absent.

Later, it was shown in [164] that the interaction of silicene with a silver substrate gives rise to energy bands at the Fermi level and silicene transformation into a metal, and the experimentally observed linear dispersion is related to hybridized electronic states localized at the interface [165].

In the case of germanene, there are a number of experimental data which allow hypothesizing the presence of a Dirac cone in it. In Ref. [150], it was shown that the density of electron states in a germanene layer on platinum is V-shaped, which is one of the signs of massless relativistic particles. In 2016, Zhang et al. [152] using scanning tunneling spectroscopy found a V-shaped dependence of the first derivative of the tunneling current with respect to voltage in germanene on MoS_2 . Nevertheless, in both cases, the density of states is nonzero at the Dirac point, which may be due to the effect of

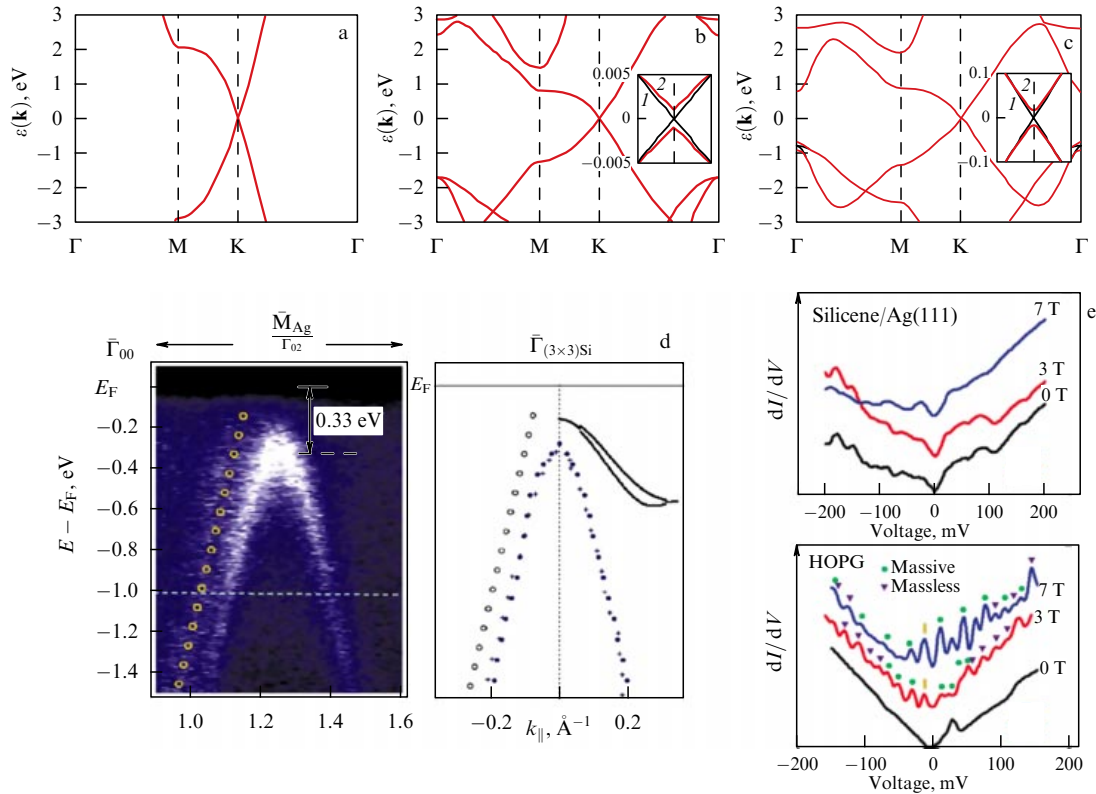


Figure 18. (Color online.) Electronic band structure of (a) graphene, (b) silicene, and (c) germanene. The insets in (b) and (c) present a comparison of electron dispersion behavior in the region of Fermi energy without considering (black color, 1) and considering (red color, 2) the spin-orbit interaction [156]. (d) Electronic structure of silicene on Ag(111) measured by the ARPES method [157]. (e) Data from scanning tunneling spectroscopy for silicene on Ag(111) and HOPG for various values of the magnetic field magnitude [163]. Triangles and dots mark the peaks whose origin is due to the Landau levels of massless and massive Dirac fermions, respectively.

the substrate on the germanene electronic structure. Thus, the Dirac electronic structure of multilayer germanene synthesized on a metal manifests itself only in layers that do not interact with it. For example, the V-shaped density of states was measured in germanene on Au(111) [166] or Cu(111) [148].

As mentioned above, the properties of silicene and germanene can be modified under external influence. It has been predicted, for instance, that a vertical electric field is capable of bandgap opening in a monolayer of silicene or germanene, transforming them from a semimetal into a semiconductor. The bandgap size both in silicene and in germanene linearly increases with the growth of the electric field strength [167]. Moreover, upon application of a vertical electric field, two Dirac cones can appear in silicene, containing bandgaps with almost 100% spin polarization, located at the corners of the Brillouin zone. Such a unique feature of the electronic structure offers a possibility of using silicene as base for a spin filter that allows switching the spin polarization of the output current by applying the electric field [168].

Also of interest are a number of theoretical papers devoted to the study of the dependence of silicene electronic properties on mechanical stress. Thus, calculations showed that its semimetallic structure (and, therefore, the Fermi velocity) is practically unchanged under a strain up to 7% [169], and under greater deformation the silicene transforms from a semimetal into a usual metal. In another paper, Wang et al. [170] predicted an effect of self-doping in silicene and germanene, caused by their deformation and implemented without introducing an impurity or bandgap opening.

Compression shifts the Fermi point in silicene and germanene below the Fermi level, as a result of which an n-doping of the system occurs, while the tensile deformation shifts the Dirac point above the Fermi level, which leads to p-doping. If the compression is directed perpendicular to the germanene plane [171], the corrugated bilayer transforms from the state of a usual metal into that of a topological insulator, the structure of which is a planar hexagonal bilayer lattice. Moreover, it is predicted that such a new phase of germanene is chemically inert.

The thermal conductivity of the structures is also substantially dependent on deformation. Xie et al. [172] theoretically showed that the silicene thermal conductivity abnormally increases under a tensile deformation because of a sharp increase in the lifetime of acoustic phonons caused by the disappearance of corrugation. Kuang et al. [173] reported that such an effect is also observed in germanene, where the tensile deformation facilitates a greater influence of the dimension effect on the thermal conductivity of the material.

4.1.4 Possible applications. In view of promising electronic properties, the main area of silicene and germanene application is electronics. In 2015, Tao et al. [174] fabricated the first field-effect transistor based on silicene operating at room temperature. Because of the effect of acoustic phonons and scattering at the grain boundaries, the measured mobility of charge carriers at room temperature amounted to $\sim 100 \text{ cm}^2 \text{ V}^{-1} \text{ s}^{-1}$ only. However, the developed approach to device fabrication has solved the main problem of saving the silicene during the transfer, which allowed applying it to

other 2D environment-sensitive films, e.g., germanene. Thus, Madhushankar et al. [175] managed to construct a field-effect transistor using germanane (hydrated germanene). The authors of the paper reported that the fabricated transistor has an on/off current ratio of $\sim 10^4$ and mobility of charge carriers of about $70 \text{ cm}^2 \text{ V}^{-1} \text{ s}^{-1}$ at room temperature.

Silicene is also promising for use in batteries. A monolayer of silicene has a high theoretical capacity of 954 mA h g^{-1} and low diffusion barrier of 0.23 eV , which leads to the expectation that it can be applied as an anode in lithium-ion batteries [176].

The authors of Ref. [177] theoretically studied the use of silicene as a sensor for such molecules as NO , NO_2 , NH_3 , and CO . It was shown that silicene possesses a high sensitivity to NO and NO_2 , rather than to NH_3 and CO . However, the latter can be detected if the pure silicene is doped with B or N atoms, thus increasing the binding energy and the electron transfer. Hussian et al. [178] reported that the introduction of vacancy defects could enhance the sensitivity of silicene to toxic gases, such as SO_2 and H_2S . The presence of defects also leads to a significant charge transfer from silicene to the gas molecules and thus affects the binding energy. Similar theoretical studies have been performed for germanene [179], where a selective sensitivity of the material to gases (NH_3 , SO_2 , and NO_2) was also observed.

4.2 Borophene

The unique electronic structure of the boron atom allows a variety of bonds in the crystalline phases, from strongly covalent two-center bonds to metal-like multicenter bonds. The latter are responsible for binding in polyhedrons dominating in crystalline boron, e.g., icosahedra B_{12} . The flexibility in the formation of bonds with different coordinations stimulated the growth of researchers' interest in boron nanostructures, including zero-dimensional (0D) clusters (fullerenes [180, 181], barrelenes [182]), 1D nanotubes [183], and 2D single-layer sheets [184].

Both theoretical and experimental studies have shown that small clusters of boron, B_n , have a tendency to take a planar shape in their ground state. The electronic structures of the clusters are like those in aromatic or antiaromatic molecules. Upon an increase in the cluster size, the closed conformers begin to compete for energy with the planar ones and become preferable over time, when the size exceeds a critical value ($n \sim 28$ in a neutral charge state). One striking example of closed boron structures is the experimentally described fullerene-like cluster B_{40} , which, according to a global energy minimum search, appears to be the ground state among the remaining 40-atom conformations [181]. This fullerene-like cluster has been studied largely due to interest in boron zero-dimensional nanostructures stimulated by the prediction of boron fullerene B_{80} [180], isoelectronic with respect to the fullerene C_{60} .

Drawing a further analogy between carbon and boron, one can imagine the structure of B_{80} as a folded two-dimensional alpha-sheet of boron, or borophene. Two-dimensional sheets of boron consist of a triangular mesh, alternated with vacancies or hollow hexagons (HH, \bigcirc) and can be formally considered an alloy $\text{B}_{1-v}\bigcirc_v$, in which the concentration of vacancies equals $v = m/N$, where m is their number in a supercell of N lattice points. Various arrangements and concentrations of HH lead to polymorphous modifications with close energies [185], the search for which is a difficult problem in combinatorics. The results of the

search for the energy minimum show that borophene stability is closely related to the concentration of HH, the effect of the substrate, and the chemical modification. The HH concentration is defined as the ratio of the number of boron atoms lacking in the HH and the number of atoms in the initial triangular sheet.

As shown in Fig. 19a [186], the energy E_f of free borophene layer formation is a nonmonotonic function having a minimum at $v = 1/9$, the form of which agrees well with other results [187]. It is interesting to note that the formation energy at two slightly greater concentrations of vacancies, $v = 1/8$ and $2/15$, is very close to the energy for $v = 1/9$. A considerable number of boron allotropes have been found, in which the formation energy is within a few meV per atom from the ground state line. This polymorphism of two-dimensional boron is substantially different from that in other 2D materials, such as graphene, h-BN, silicene, or germanene (described above) that have a honeycomb structure.

In borophene, the atoms in the centers of hexagons serve as 'donors', whereas HHs act as 'acceptors' [189], the interaction of which compensates the electron deficiency in boron [190]. If the three valence electrons of each 'donor' boron atom are completely shared with the hexagonal base (colored white in the inset in Fig. 19a), then it will be isoelectronic with respect to graphene. This simple mechanism explains why the layer with $v = 1/9$ is among the preferable structures (Fig. 19a, curve 1). With some secondary factors taken into account, such as vacancy–vacancy interaction (such interaction is enhanced, e.g., for double vacancies), the ground state can be a polymorphous modification with a somewhat higher value of $v \approx 1/8$. The boron layers with $v < 1/9$ are electron-redundant and demonstrate out-of-plane bending due to the mixing of in-plane and out-of-plane orbitals, while the same sheets with $v > 1/9$ are perfectly planar [185]. The boron layer with high v is electron deficient and has a tendency to draw electrons from the substrate to stabilize its structure. An extreme example is graphene-like borophene ($v = 1/3$), unstable in a vacuum but having an energy minimum on some substrates due to the electron transfer from metallic layers (which was observed experimentally; see Section 4.2.1).

The decisive role of the substrate for borophene structure is determined by the fact that, in contrast to, e.g., graphene or h-BN, 2D boron has a much higher energy than its crystalline form. To organize boron in two-dimensional structures, it was proposed in several theoretical studies [186, 191] to use metallic Ag and Cu substrates for the removal of degeneracy of the polymorphous energy and kinetic direction of boron sheet growth. Indeed, the ground states of borophene are different in a free state and on substrates (Fig. 19a). On a surface of Ag(111), the borophene phase with $v = 1/6$ is the most stable. The second and the third most stable structures appear at $v = 1/8$ and $v = 1/12$ (Fig. 19b). The corresponding energy difference between the second and the third most stable structures and the ground state ($v = 1/6$) is only 0.4 and 2.1 meV per atom, respectively [186], which evidences the conservation of borophene polymorphism on the Ag(111) surface. A similar situation occurs in the case of the Au(111) surface (Fig. 19a, blue curve 2). In the case of synthesis on Ni(111), polymorphous modifications with various values of v are also energetically preferable, but the energy difference between the ground state and the next ones increases. However, on a Cu(111) surface, the minimal energy of

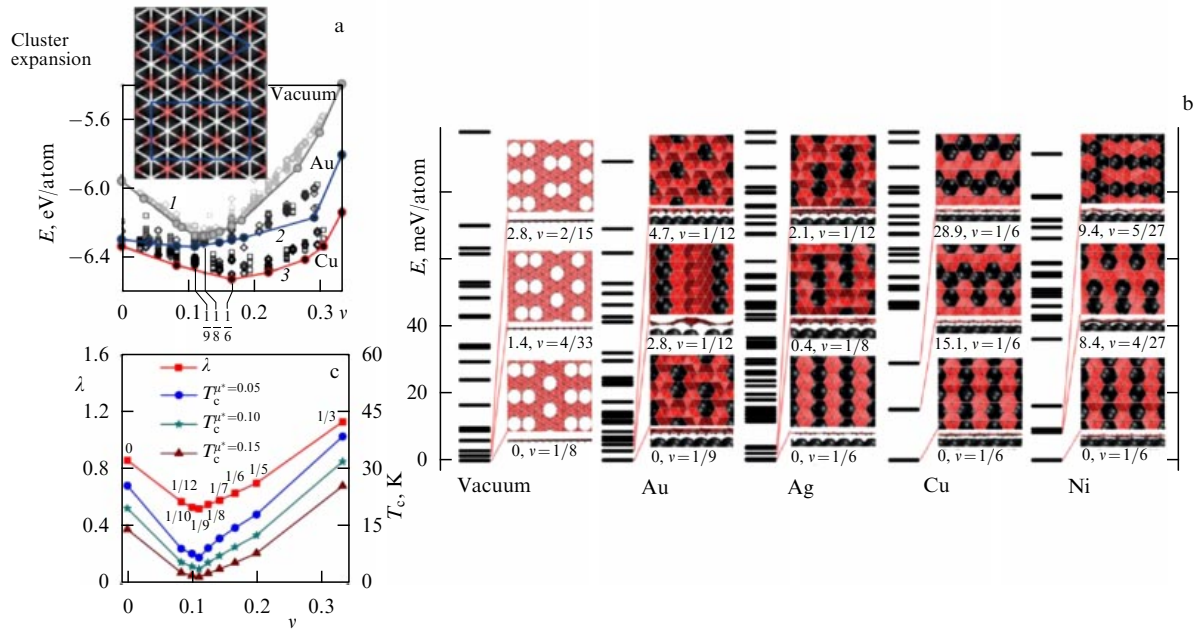


Figure 19. (Color online.) (a) Dependence of energy of all nonequivalent borophene sheets ($B_{1-v}\bigcirc_v$) on the concentration of hollow hexagons (v) in a vacuum, as well as on Au and Cu substrates [186]. (b) Energy spectra of various borophene modifications in a freestanding state, as well as on Au, Ag, Cu, and Ni surfaces. In the insets, each column presents the three most stable structures and indicates their energy with respect to the ground state (meV per atom) and the value of v [186]. (c) The temperature of a transition to the superconducting state (for different values of the Coulomb pseudopotential μ^*) and the constants of electron-phonon coupling λ versus the concentration of hollow hexagons (vacancies) in a free layer [188].

formation belongs to layers with $v = 1/6$ (Fig. 19a, red curve 3), the energy difference between the ground state and the next ones being 15.1 and 28.9 meV per atom, which is significantly higher than on the Ag(111) surface (Fig. 19b). This observation evidences the actual removal of degeneracy in energy for different v in the case of borophene synthesis on the Cu(111) surface and a reduction in structural polymorphism.

4.2.1 Borophene synthesis. The described theoretical prognoses were later confirmed in a number of experiments, the structures obtained having indeed demonstrated polymorphism. So, for example synthesis on various metallic substrates under high vacuum conditions was reported for the following phases: $v = 0$ (Ag [192]), $v = 1/12$ (Au [192]), $v = 1/6$, $v = 1/5$ (Ag [184, 194, 195]), and the graphene-like borophene phase ($v = 1/3$) on Al [196].

In the synthesis of borophene with $v = 0$ on Ag [92], an STM analysis showed the corrugation of the structure with an amplitude of ~ 0.8 Å, which corresponds to theoretical predictions for boron layers with $v < 1/9$ [185]. On the other hand, in [197] it was proved that for the Ag(111) substrate the structure with $v = 1/6$ (lower in energy by 42 meV per atom) rather than with $v = 0$ is an energetically preferable phase. Later, in review [198], the hypothesis was put forward again that in experiment [192] exactly the polymorphous modification with $v = 1/6$ could have been synthesized. The authors showed that the layer with $v = 1/6$ has high flexibility and is able to repeat the periodic corrugation of the reconstructed surface Ag(111). Such a corrugated layer with $v = 1/6$ can explain well the experimentally observed corrugated phase [192] from the point of view of topography, wavelength, moiré pattern, and HH distribution. The modeled STM image [198] also coincides well with the experimental one [192].

Two phases of borophene with $v = 1/6$ and $v = 1/5$ were synthesized on the substrate Ag(111) [184, 194, 195]. These two polymorphous modifications are planar without vertical waves with variously adjacent HHs.

Reference [196] confirmed the theoretical hypothesis [186] that graphene-like borophene ($v = 1/3$) can be synthesized on a substrate that ensures intense charge transfer. Indeed, the redistribution of charge from the Al(111) substrate to graphene-like borophene amounts to almost an electron, whereas the silver substrate used in other studies leads to a minor charge transfer.

In spite of the fact that experiment [184] showed a relative stability of borophene with respect to oxidation (the structure degradation occurs mainly at the reactive edges of boron islands), long-term action of the environment [192] affects the structure. This fact agrees with the above prognosis, according to which the boron layers on metals are sufficiently reactive and may serve as catalysts of the hydrogen release reaction [186]. However, this does not mean less structural stability of borophene as compared to other 2D films. Recently, it was shown experimentally that the surface of some dichalcogenides of transition metals, earlier considered inert, are also subject to oxidation [199].

4.2.2 Mechanical properties of borophene. The combination of covalent and metal-like multicenter bonds in borophene gives rise to its unique mechanical properties [198]. The two-dimensional elastic modulus of borophene demonstrates high anisotropy, and its magnitude in some modifications is record breaking. So, the elastic modulus of the hexagonal polymorphous modification with $v = 0$ along the armchair direction can attain 398 N m^{-1} [192], which is greater than in graphene (345 N m^{-1} [92]) and in any other material, and this result was obtained as early as 2006 [200]. However, the authors of Ref. [200] expressed the value in standard units,

characterizing the elastic modulus of a three-dimensional material, having multiplied the 2D value by an arbitrary chosen thickness of a two-dimensional borophene film. The resulting value of 0.87 TPa appeared smaller than the graphene elastic modulus of 1.06 TPa (this value can be correctly converted from 2D to 3D, since the thickness of the graphene film is physically substantiated and corresponds to the distance between the individual atomic layers in graphite). In this case, expressing the value found by the authors of Ref. [200] in units of N m^{-1} yields 367 N m^{-1} , which is close to the data in Ref. [192]. Thus, an incorrect interpretation did not allow timely predicting the record-breaking stiffness of borophene, which could possibly slow its further synthesis and thorough investigation. Note that, due to its corrugated structure, the polymorphous modification with $\nu = 0$ also has a negative Poisson coefficient (-0.04 in the armchair direction and -0.02 in the zigzag direction). Besides the polymorphous modification with $\nu = 0$, elastic moduli exceeding those in graphene are inherent in borophenes with $\nu = 1/9$ (618.93 N m^{-1}) and $\nu = 1/7$ (545.62 N m^{-1}) [201].

Borophene-based structures are usually rather flexible. The bending modulus of a layer with $\nu = 1/6$ is only 0.39 eV along the HH rows, which is one fourth of the corresponding value in graphene, and increases to 0.56 eV in HH rows, demonstrating greater anisotropy than the in-plane elastic moduli [202]. In all other layers of boron with HH, although having higher bending stiffness, these values are still substantially lower than in graphene. The excellent in-plane mechanical stiffness and unusual out-of-plane flexibility open the possibility of using the two-dimensional boron layers as a reinforcing component in up-to-date composites. On the other hand, the layer with $\nu = 0$ has exclusively high bending modulus along one of the directions (4.9 eV) because of the corrugated structure.

Of particular interest is the ideal strength of borophene. It was shown that the layer with $\nu = 1/6$ has an ideal strength of $14\text{--}15 \text{ N m}^{-1}$, close to the corresponding value for MoS_2 [203] and substantially exceeding the values for phosphorene [204] and silicene [205]. The value of the critical strain is within the range of $10\text{--}15\%$ [202, 206], which is slightly lower than in graphene ($\sim 25\%$). Under critical deformation, two-dimensional boron is not destroyed but experiences a structural phase transition. As the tensile deformation increases, the boron atoms tend to reorganize in a way extending the sheet area by increasing the HH concentration, which decreases the tension. The structure phase transition can additionally strengthen the material to such a degree that it will be able to sustain great loads even when extremely tensioned. The key role of HHs is seen from the fact that the structure of polymorphous borophene modification without HH ($\nu = 0$) is fragile with the limit deformation of 8% (for tension along the ridges) [202].

4.2.3 Electronic properties of borophene. All polymorphous modifications of borophene were predicted to exhibit metallic properties [185, 187]. Experiment [207] using ARPES confirmed the prognosis for the case of a polymorphous modification of borophene with $\nu = 1/6$ on an Ag(111) substrate.

The small mass of a boron atom suggests the presence of a strong electron–phonon coupling, which, together with the metallicity inherent in borophene, can lead to superconductivity. The superconductive properties of borophene were

described in a number of papers [188, 208–214]. In particular, it was shown in [188] that the temperature of the transition to superconductive state changes nonlinearly, and its dependence on ν has the same form as the dependence of the energy of formation of polymorphous borophene modifications (see Fig. 19a, c) and can reach 40 K for the case of graphene-like borophene (the minimal critical temperature $T_c = 4 \text{ K}$ corresponds to $\nu = 1/9$). This behavior is related to the fact that the electron density of states at the Fermi level and the electron–phonon coupling constant (λ) have a similar dependence due to the changing contribution of σ -orbitals to the Fermi surface.

Also worth noting is the substantial dependence of T_c on the mechanical strain and the degree of doping [214]. In particular, it was shown that the compressive deformation and the electron doping decrease T_c in the polymorphous borophene modification with $\nu = 0$. Moreover, for the case of polymorphous modification with $\nu = 1/6$, it was theoretically found in [213] that the electron doping of 0.1e per boron atom decreases T_c from 14 to 0.09 K. This explains the difficulty of superconductivity experimental detection in borophene, because it is usually synthesized on metallic substrates that dope the system. Thus, the borophene synthesized on Ag, Al, Cu, or Ni under the action of electron doping possesses a lower temperature of transition to the superconductive state, whereas when synthesized on Au it will be doped with holes and, correspondingly, characterized by higher values of T_c [198].

4.2.4 Possible applications. The small mass and perfect mechanical characteristics of two-dimensional boron can be useful in up-to-date composites. On the one hand, two-dimensional boron can sustain a load comparable to that for graphene. On the other hand, the reactivity of two-dimensional boron facilitates covalent bonding with the surrounding matrix, which ensures an efficient load transfer.

As the lightest 2D material, borophene is rather promising for hydrogen power engineering and according to theoretical estimates [215] is capable of providing a superhigh hydrogen storage capacity. Although the boric system is chemically more active than graphene, it demonstrates an energy of binding with hydrogen ($\sim 0.05 \text{ eV}$) insufficient for its storage at room temperature [215]. This problem could be solved by decorating the boron structure with metal atoms. Indeed, earlier it was found that molecular hydrogen interacting with metals forms an intermediate type of bond, so-called Kubas and anti-Kubas interactions. The Kubas interaction [216] is due to the electron interchange between H_2 molecules and unfilled d-orbitals of transition metal atoms, as well as between electrons in transition metal atoms and the anti-bonding orbitals of H_2 . The anti-Kubas interaction [217], in contrast to the previous one, is related to the polarization of a hydrogen molecule by a metal atom, which leads to its attachment to the metal in a quasi-molecular form [218]. Intermediate-type interactions seem most promising for hydrogen adsorption, since their binding energy amounts to $\sim 10^{-1} \text{ eV}$ [219].

Indeed, the boric nanostructure with metallic atoms adsorbed on it demonstrates an acceptable molecular hydrogen adsorption energy per atom of metal. Thus, it was found that dispersion of alkali metal atoms (Li, Na, and K) on a boron sheet considerably increases the energy of hydrogen bonding and storage capacity. The two-dimensional boron in this case ensures the attachment of metal atoms separated by

a large distance, which prevents their clustering [215]. For example, when decorating borophene with Li atoms, the adsorption energy of the H_2 molecule attains 0.35 eV, and up to three hydrogen molecules can be adsorbed on each atom of Li, which is equivalent to a hydrogen storage capacity of 10.8 wt.% [215].

It is theoretically predicted that borophene with $\nu = 1/9$ decorated with atoms of Ca and Sc is a perfect adsorbent for capturing CO_2 molecules from the environment, the adsorption energy approaching 3.0 eV [220, 221]. For negatively charged borophene with $\nu = 1/6$, the CO_2 sorption capacity amounts to $6.73 \times 10^{14} \text{ cm}^{-2}$, the process being reversible. So, the process of adsorbing/desorbing CO_2 can be controlled by changing the borophene doping.

Other theoretical work also showed that boron sheets are a promising material with attractive electrochemical properties for both Li-ion and Na-ion batteries [222–226]. The borophene phase with $\nu = 0$ was found to interact strongly with clusters having the composition Li_xS_y , which leads to their decomposition and irreversible loss of sulphur during the charging/discharging processes [225]. On the other hand, the interaction between Li-S and borophene with $\nu = 1/5$ [225] and $1/6$ [226] is much weaker than in the case of the polymorphous modification with $\nu = 0$, but greater than between Li-S and graphene. This shows that the considered phases of borophene are a suitable base for lithium-sulfur batteries [227].

It is worth noting that with the attachment of metal atoms borophene can undergo a structural phase transition because of doping with electrons from adsorbates, which, therefore, requires further detailed structural investigations [198].

Borophene is the lightest catalyst of the hydrogen extraction reaction, with almost zero free energy of hydrogen adsorption, metallic conductivity, and large number of active centers on the surface [228, 229]. For the borophene phase with $\nu = 0$, the interaction between the H atom and borophene is too strong because of high surface activity. For the phase with $\nu = 1/5$, the role of active centers is played by the 5-coordinated boron atoms. This leads to the fact that the free energy of hydrogen adsorption is only 0.02 eV, even closer to zero than on Pt (–0.09 eV) [227]. For the phase with $\nu = 1/6$, the 4-coordinated boron atoms are the best active centers, the corresponding free energy of hydrogen adsorption amounting to only 0.1 eV. A small amount of free energy of hydrogen adsorption was also found in polymorphous modifications with $\nu = 1/9$ and $1/8$. Borophene retains its high catalytic activity on a substrate of silver as well [230].

4.3 Two-dimensional films of other elements of groups 13–16

Besides the two-dimensional films described above, films of other compositions of the considered elements of groups 13–16 have been obtained experimentally; however, their detailed studies are still in progress. In this section, we will only briefly dwell on the properties of some materials known to date.

Kochat et al. presented a technique for isolating thin gallium-based films (gallenene, Fig. 20a, b) by exfoliation from a droplet of a melted bulk crystal on a silicon substrate at room temperature [231]. The calculations of the gallene electronic structure showed the presence of a partially filled Dirac cone and a nonlinear dispersion band near the Fermi level, which allowed a conclusion about the metallic character of the two-dimensional material, as was earlier shown for some other two-dimensional crystals of group 13 (borophene,

aluminene). Furthermore, in the paper it was noted that, at the expense of strong interaction of 2D Ga with the semiconductor MoS_2 , the latter can also exhibit metallic properties, and a heterostructure based on these materials offers new prospects in the field of plasmonics and nanosensors.

Two-dimensional Sn (stanene, a two-dimensional counterpart of the tin crystal, Fig. 20c–f) became a subject of thorough study both in experiment and in theory due to a hypothetical possibility of using it as a topologic insulator at room temperature, as well as a spin filter in devices operating at the expense of a huge magnetoresistance effect [237, 238]. Zhu et al. [233] demonstrated the possibility of growing stanene as thin as 3.5 Å with a curved two-dimensional lattice on a substrate of bismuth telluride by the method of molecular beam epitaxy, as well as the presence of a bandgap within the metallic states. Reference [232] demonstrated the possibility of stanene stabilization in a perfectly planar state on a metallic Cu(111) surface, where the opening of a topologic bandgap of 0.3 eV was also observed.

Electronic properties were also studied in stanene nanoribbons. In particular, semiconductor properties are observed both in pure ribbons and in those with the edges passivated with hydrogen. At the same time, the spin-orbit coupling differently depends of the type of the ribbon edges: in ‘zigzag’ nanoribbons the bandgap width increases and, on the contrary, in ‘armchair’ ones it decreases. Theoretical calculations of the magnetic properties of nanoribbons revealed their ferromagnetic ground state with opposite directions of spins at the edges [239].

It is interesting to note that the adsorption of transition metal atoms on a stanene surface highly affects the electronic and magnetic properties. Thus, Xing et al. have shown that stanene is a semiconductor under the adsorption of Fe, a semimetal in the case of Co, and exhibits metallic properties under the adsorption of V, Cr, Mn, and Cu on the surface. Whereas the magnetic moments on atoms of Ni, Cu, and Zn are preserved, 2D Sn becomes nonmagnetic [240]. Wang et al. [241] predicted the manifestation of the quantum Hall effect in stanene under the action of a compressive or tensile strain.

New two-dimensional allotropic forms were predicted for the elements of group 16, Te (Fig. 20g–j) and Se (Fig. 20k–n), including their spiral-shaped configuration of covalently bound atoms, twisted around the c -axis [242]. Simultaneously, Zhu et al. and Xian et al. independently published theoretical papers on the study of new phases of 2D Te (tellurene) with differing estimates of their stability [235, 243]. Xian et al. [243] supposed that the most stable allotropic form of Se and Te is a 1D spiral-shaped chain (the structure cell of a bulk crystal). However, they showed that such two-dimensional compounds as ‘rectangular tellurene’ and ‘square tellurene’ have a cohesion energy of 0.06 eV and 0.13 eV per atom, respectively, which is greater than the analogous value for 1D spirals. Such ‘rectangular’ lattices of selenene and tellurene have a corrugated structure (by analogy with the 2D films of other monocompounds investigated earlier), which can be additionally stabilized, e.g., under the conditions of epitaxial growth on a substrate of Au. Zhu et al. [235] predicted three possible 2D reconstructions of the tellurene surface for a fixed set of thicknesses with the number of atoms $N = 3, 6, 9, 12$, and 15: a stable hexagonal α -Te lattice, metastable rectangular β -Te lattice, and metastable hexagonal γ -Te lattice. The nature of such

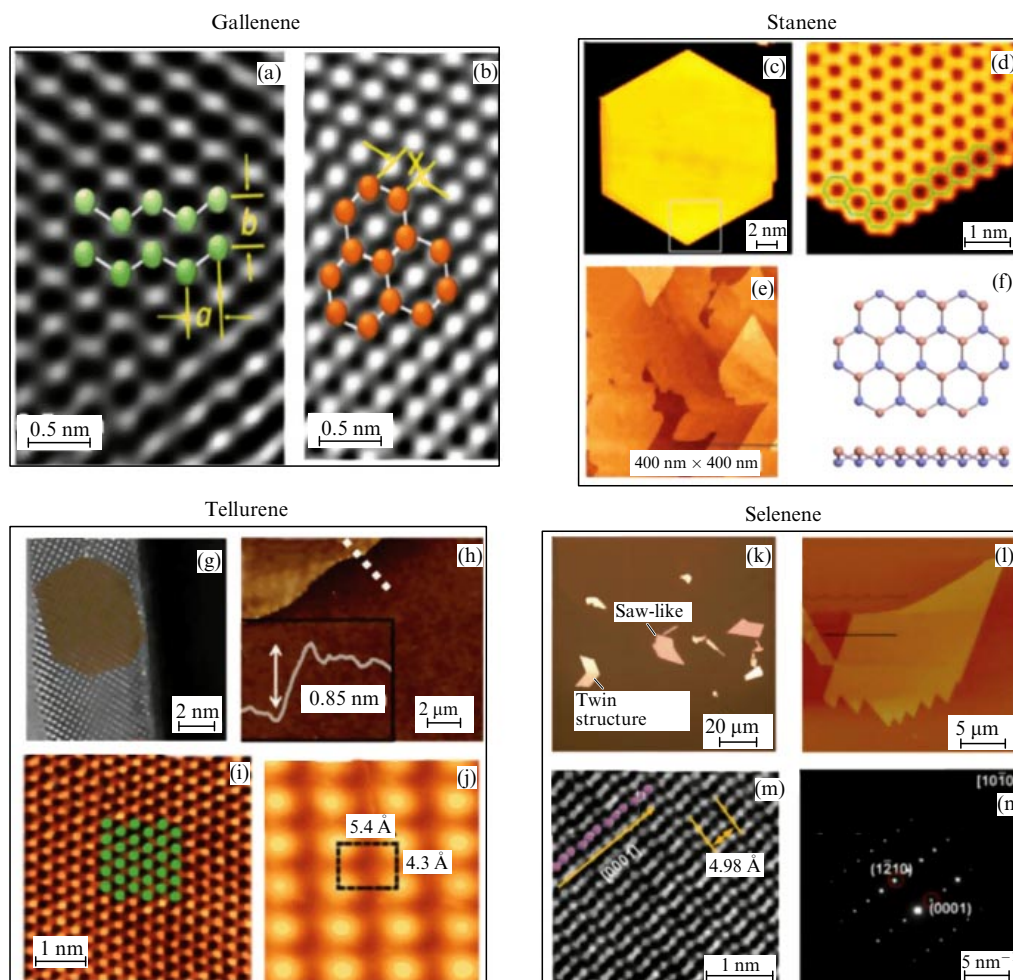


Figure 20. (a, b) TEM images of gallenene layers and their atomic structure [231]. (c) STM image of a stanene hexagonal cluster and (d) its magnification in the zone marked by the white square [232]. (e) STM image of a stanene film and the corresponding (f) atomic model, top and side view [233]. (g) High-resolution TEM image of a 6-nm tellurene film on MgO(100). (h) AFM image and the height profile (inset) of a tellurene fragment 0.85 nm thick and (i) STEM image of one of the observed polymorphs of tellurene [234]. (j) STM image of a tellurene film on graphene [235]. (k) Optical microscopy image and (l) the corresponding AFM height profile of a saw-like area of silicene film. (m) STEM image of selenene and (n) electron diffraction data from the corresponding area [236].

unusual restrictions on the film thickness (e.g., $N = 3$) is explained by the multivalence of Te atoms, in which the central atoms demonstrated the metallic character of bonding (σ -bonds) and the two outer atoms were bound via the donor-acceptor mechanism.

5. Conclusion

The present review elucidates only a small part of the vast class of two-dimensional nanomaterials intensely studied to date. Nevertheless, the presented and generalized results clearly demonstrate the prospects of further studies in this field.

Thus, special attention was paid to the description of new methods of synthesis of two-dimensional structures, such as stabilization of 2D films in a matrix of other two-dimensional materials (e.g., the growth of a d-metal film in a graphene pore or a new phase formation in an MoSe₂ matrix) or between layers, as shown for 2D lithium. The revealed outstanding mechanical, electronic, magnetic, and optical properties of the films studied can find wide application in electronics, spintronics, photovoltaics, photocatalysis, gas

sensors, and many other fields of fundamental and applied research.

The review shows that the field of two-dimensional materials is still in the active stage of formation. The available experimental data are sometimes incomplete, and theoretical studies may not always unambiguously explain the origin of the observed processes and phenomena. The authors sincerely hope that the present review will keep the interest of a wide community of readers alive regarding both the further accumulation of knowledge on the structure and properties of a wide class of already known two-dimensional atomically thin films and the synthesis, prediction, and investigation of new compounds.

Acknowledgments

The work was supported by the Russian Science Foundation (project no. 17-72-20223).

References

1. Novoselov K S et al. *Proc. Natl. Acad. Sci. USA* **102** 10451 (2005)
2. Novoselov K S et al. *Nature* **490** 192 (2012)

3. Morozov S V, Novoselov K S, Geim A K *Phys. Usp.* **51** 744 (2008); *Usp. Fiz. Nauk* **178** 776 (2008)
4. Morozov S V *Phys. Usp.* **55** 408 (2012); *Usp. Fiz. Nauk* **182** 437 (2012)
5. Ferrari A C et al. *Nanoscale* **7** 4598 (2015)
6. Sorokin P B, Chernozatonskii L A *Phys. Usp.* **56** 105 (2013); *Usp. Fiz. Nauk* **183** 113 (2013)
7. Singh A K, Yakobson B I *Nano Lett.* **9** 1540 (2009)
8. Ribas M A et al. *Nano Res.* **4** 143 (2011)
9. Chernozatonskii L A et al. *JETP Lett.* **85** 77 (2007); *Pis'ma Zh. Eksp. Teor. Fiz.* **85** 84 (2007)
10. Chernozatonskii L A, Sorokin P B, Brüning J W *Appl. Phys. Lett.* **91** 183103 (2007)
11. Chernozatonskii L A, Sorokin P B *J. Phys. Chem. C* **114** 3225 (2010)
12. Nilsson L et al. *Carbon* **50** 2052 (2012)
13. Chernozatonskii L A, Sorokin P B, Artukh A A *Russ. Chem. Rev.* **83** 251 (2014); *Usp. Khim.* **83** 251 (2014)
14. Glavin N R et al. *Adv. Mater.* **32** 1904302 (2020)
15. Ferrari A, Stephens M “So many materials” *Phys World* (Focus on Nanotechnology) (2018), Marris Stephens (Physics World) interviews Andrea Ferrari (Director of the Cambridge Graphene Centre), <https://physicsworld.com/a/so-many-materials/>
16. Mounet N et al. *Nat. Nanotechnol.* **13** 246 (2018)
17. Zhou J et al. *Sci. Data* **6** 86 (2019)
18. Ling X et al. *Proc. Natl. Acad. Sci. USA* **112** 4523 (2015)
19. Lew Yan Voon L C, Guzmán-Verri G G *MRS Bull.* **39** 366 (2014)
20. Algara-Siller G et al. *Nature* **519** 443 (2015)
21. Björkman T et al. *Sci. Rep.* **3** 3482 (2013)
22. Bakharev P V et al. *Nat. Nanotechnol.* **15** 59 (2020)
23. Puthirath Balan A et al. *Nat. Nanotechnol.* **13** 602 (2018)
24. Naguib M et al. *Adv. Mater.* **26** 992 (2014)
25. Zhao J et al. *Science* **343** 1228 (2014)
26. Shao Y, Pang R, Shi X J *J. Phys. Chem. C* **119** 22954 (2015)
27. Larionov K V, Kvashnin D G, Sorokin P B *J. Phys. Chem. C* **122** 17389 (2018)
28. Wang P, Wang H, Yang W *RSC Adv.* **4** 17008 (2014)
29. Thomsen M R, Brun S J, Pedersen T G *Phys. Rev. B* **91** 125439 (2015)
30. Kim K H et al. *Adv. Mater. Interfaces* **7** 1902104 (2020)
31. Zhang T et al. *Nat. Phys.* **6** 104 (2010)
32. Hoang V V et al. *Comput. Mater. Sci.* **126** 446 (2017)
33. Chen S, Zeng X C *ACS Appl. Mater. Interfaces* **9** 12100 (2017)
34. Yang W, Wang H *Procedia IUTAM* **10** 273 (2014)
35. Zhao X et al. *Adv. Mater.* **30** 1707281 (2018)
36. Sutter E et al. *Nano Lett.* **16** 4410 (2016)
37. Joseph T et al. *J. Phys. Chem. Lett.* **10** 6492 (2019)
38. Yang L-M, Frauenheim T, Ganz E *Phys. Chem. Chem. Phys.* **17** 19695 (2015)
39. Yang L-M et al. *Phys. Chem. Chem. Phys.* **17** 26036 (2015)
40. Koskinen P, Korhonen T *Nanoscale* **7** 10140 (2015)
41. Antikainen S, Koskinen P *Comput. Mater. Sci.* **131** 120 (2017)
42. Wang X et al. *Nano Lett.* **19** 4560 (2019)
43. Nevalaita J, Koskinen P *Nanoscale* **11** 22019 (2019)
44. Bampoulis P et al. *J. Phys. Chem. C* **120** 27079 (2016)
45. Šljivančanin Ž, Belić M *Phys. Rev. Mater.* **1** 044003 (2017)
46. Kühne M et al. *Nature* **564** 234 (2018)
47. Larson D T et al. *Phys. Rev. B* **101** 075407 (2020)
48. Chepkasov I V et al. *Nano Energy* **75** 104927 (2020)
49. Liu X-C et al. *Sci. Adv.* **6** eaay4092 (2020)
50. Geim A K, Grigorieva I V *Nature* **499** 419 (2013)
51. Liu W Q et al. *Sci. Rep.* **5** 11911 (2015)
52. Zhou G *Phys. Chem. Chem. Phys.* **22** 667 (2020)
53. Choi J I et al. *Adv. Funct. Mater.* **29** 1902274 (2019)
54. Biswas A et al. *Adv. Colloid Interface Sci.* **170** 2 (2012)
55. Chernozatonskii L A et al. *JETP Lett.* **90** 134 (2009); *Pis'ma Zh. Eksp. Teor. Fiz.* **90** 144 (2009)
56. Kvashnin A G et al. *Nano Lett.* **14** 676 (2014)
57. Kvashnin A G, Sorokin P B *J. Phys. Chem. Lett.* **5** 541 (2014)
58. Kvashnin A G et al. *J. Phys. Chem. Lett.* **7** 2659 (2016)
59. Claeysens F et al. *J. Mater. Chem.* **15** 139 (2005)
60. Freeman C L et al. *Phys. Rev. Lett.* **96** 066102 (2006)
61. Goniakowski J, Noguera C, Giordano L *Phys. Rev. Lett.* **98** 205701 (2007)
62. Sorokin P B et al. *Nano Lett.* **14** 7126 (2014)
63. Kvashnin A G, Sorokin P B, Tománek D J *Phys. Chem. Lett.* **5** 4014 (2014)
64. Goniakowski J, Noguera C, Giordano L *Phys. Rev. Lett.* **93** 215702 (2004)
65. Hernandez Y et al. *Nat. Nanotechnol.* **3** 563 (2008)
66. Tikhomirova K A et al. *J. Phys. Chem. Lett.* **11** 3821 (2020)
67. Lin S S J *Phys. Chem. C* **116** 3951 (2012)
68. Tsipas P et al. *Appl. Phys. Lett.* **103** 251605 (2013)
69. Tusche C, Meyerheim H L, Kirschner J *Phys. Rev. Lett.* **99** 026102 (2007)
70. Mansurov V et al. *J. Cryst. Growth* **428** 93 (2015)
71. Hong H-K et al. *Nano Lett.* **17** 120 (2017)
72. Quang H T et al. *ACS Nano* **9** 11408 (2015)
73. Lee J, Sorescu D C, Deng X J *J. Phys. Chem. Lett.* **7** 1335 (2016)
74. Wang Z L J *Phys. Condens. Matter* **16** R829 (2004)
75. Fan Z, Lu J G J *Nanosci. Nanotechnol.* **5** 1561 (2005)
76. Sahoo T et al. *Mater. Res. Bull.* **75** 134 (2016)
77. Pan Q et al. *Catal. Lett.* **144** 648 (2014)
78. Deng X et al. *J. Phys. Chem. C* **117** 11211 (2013)
79. Shiotari A et al. *J. Phys. Chem. C* **118** 27428 (2014)
80. Weirum G et al. *J. Phys. Chem. C* **114** 15432 (2010)
81. Martynova Y et al. *J. Catal.* **301** 227 (2013)
82. Topsakal M et al. *Phys. Rev. B* **80** 235119 (2009)
83. Guo H et al. *J. Phys. Chem. C* **116** 11336 (2012)
84. Li C et al. *Appl. Phys. Lett.* **90** 223102 (2007)
85. Tu Z C, Hu X *Phys. Rev. B* **74** 035434 (2006)
86. Tu Z C J *Comput. Theor. Nanosci.* **7** 1182 (2010)
87. Blonsky M N et al. *ACS Nano* **9** 9885 (2015)
88. Peng Q et al. *Comput. Mater. Sci.* **68** 320 (2013)
89. Wei X et al. *Phys. Rev. B* **80** 205407 (2009)
90. Sai N, Mele E J *Phys. Rev. B* **68** 241405(R) (2003)
91. Kvashnin D G et al. *J. Phys. Chem. Lett.* **9** 5086 (2018)
92. Kudin K N, Scuseria G E, Yakobson B I *Phys. Rev. B* **64** 235406 (2001)
93. Hu W, Li Z, Yang J J *Chem. Phys.* **138** 124706 (2013)
94. Yao Q et al. *RSC Adv.* **4** 17478 (2014)
95. Kvashnin A G, Sorokin P B, Chernozatonskii L A *Comput. Mater. Sci.* **142** 32 (2018)
96. Kano E et al. *Nanoscale* **9** 3980 (2017)
97. Yin K et al. *2D Mater.* **4** 011001 (2017)
98. Heinemann M, Eifert B, Heiliger C *Phys. Rev. B* **87** 115111 (2013)
99. Kvashnin D G et al. *J. Phys. Chem. C* **123** 17459 (2019)
100. Fan D et al. *ACS Appl. Mater. Interfaces* **12** 30297 (2020)
101. Zhang Z et al. *J. Am. Chem. Soc.* **134** 19326 (2012)
102. Xu B et al. *Nanoscale* **10** 215 (2018)
103. Fan D et al. *J. Mater. Chem. C* **5** 3561 (2017)
104. Larionov K V et al. *JETP Lett.* **108** 13 (2018); *Pis'ma Zh. Eksp. Teor. Fiz.* **108** 14 (2018)
105. Zhu C et al. *J. Mater. Chem. C* **7** 6406 (2019)
106. Larionov K V, Seifert G, Sorokin P B *Nanoscale* **12** 13407 (2020)
107. Takeda K, Shiraishi K *Phys. Rev. B* **50** 14916 (1994)
108. Cahangirov S et al. *Phys. Rev. Lett.* **102** 236804 (2009)
109. Jose D, Datta A J *Phys. Chem. C* **116** 24639 (2012)
110. Meng L et al. *Nano Lett.* **13** 685 (2013)
111. Chiappe D et al. *Adv. Mater.* **26** 2096 (2014)
112. Aizawa T, Suehara S, Otani S J *J. Phys. Chem. C* **118** 23049 (2014)
113. Stepniak-Dybala A, Krawiec M J *J. Phys. Chem. C* **123** 17019 (2019)
114. Huang L et al. *Nano Lett.* **17** 1161 (2017)
115. De Crescenzi M et al. *ACS Nano* **10** 11163 (2016)
116. Feng B et al. *Nano Lett.* **12** 3507 (2012)
117. Vogt P et al. *Phys. Rev. Lett.* **108** 155501 (2012)
118. Chen L et al. *Phys. Rev. Lett.* **110** 085504 (2013)
119. Arafune R et al. *Surf. Sci.* **608** 297 (2013)
120. Salomon E et al. *J. Phys. Condens. Matter* **26** 185003 (2014)
121. Grazianetti C et al. *J. Phys. Condens. Matter* **27** 255005 (2015)
122. Jamgotchian H et al. *J. Phys. Condens. Matter* **27** 395002 (2015)
123. Hsu H-C et al. *Semicond. Sci. Technol.* **33** 075004 (2018)
124. De Padova P et al. *J. Phys. Condens. Matter* **24** 223001 (2012)
125. Enriquez H et al. *J. Phys. Condens. Matter* **24** 314211 (2012)
126. Sheng S et al. *Nano Lett.* **18** 2937 (2018)
127. Jamgotchian H et al. *J. Phys. Condens. Matter* **24** 172001 (2012)
128. Chiappe D et al. *Adv. Mater.* **24** 5088 (2012)

129. Vogt P et al. *Appl. Phys. Lett.* **104** 021602 (2014)
130. Sheverdyaeva P M et al. *ACS Nano* **11** 975 (2016)
131. Liu Z-L et al. *New J. Phys.* **16** 075006 (2014)
132. Resta A et al. *Sci. Rep.* **3** 2399 (2013)
133. De Padova P et al. *J. Phys. Chem. C* **121** 27182 (2017)
134. Grazianetti C, Molle A, in *GraphITA: Selected Papers from the Workshop on Synthesis, Characterization and Technological Exploitation of Graphene and 2D Materials Beyond Graphene* (Eds V Morandi, L Ottaviano) (Cham: Springer Intern. Publ., 2017) p. 137
135. Lin C-L et al. *Appl. Phys. Exp.* **5** 045802 (2012)
136. Lalami B et al. *Appl. Phys. Lett.* **97** 223109 (2010)
137. Wu K-H *Chinese Phys. B* **24** 086802 (2015)
138. Chen L et al. *Phys. Rev. Lett.* **109** 056804 (2012)
139. De Padova P et al. *Appl. Phys. Lett.* **102** 163106 (2013)
140. De Padova P et al. *J. Phys. Condens. Matter* **25** 382202 (2013)
141. Moras P et al. *J. Phys. Condens. Matter* **26** 185001 (2014)
142. Lee G-W, Chen H-D, Lin D-S *Appl. Surf. Sci.* **354** 187 (2015)
143. Dávila M E et al. *New J. Phys.* **16** 095002 (2014)
144. Li F et al. *J. Phys. D* **50** 115301 (2017)
145. Zhuang J et al. *ACS Nano* **11** 3553 (2017)
146. Derivaz M et al. *Nano Lett.* **15** 2510 (2015)
147. Stephan R et al. *J. Phys. Chem. C* **120** 1580 (2016)
148. Qin Z et al. *Adv. Mater.* **29** 1606046 (2017)
149. Bampoulis P et al. *J. Phys. Condens. Matter* **26** 442001 (2014)
150. Zhang L et al. *Appl. Phys. Lett.* **107** 111605 (2015)
151. d'Acapito F et al. *J. Phys. Condens. Matter* **28** 045002 (2016)
152. Zhang L et al. *Phys. Rev. Lett.* **116** 256804 (2016)
153. Persichetti L et al. *J. Phys. Chem. Lett.* **7** 3246 (2016)
154. Liu C-C, Feng W, Yao Y *Phys. Rev. Lett.* **107** 076802 (2011)
155. Yao Y et al. *Phys. Rev. B* **75** 041401(R) (2007)
156. Matthes L, Pulci O, Bechstedt F *J. Phys. Condens. Matter* **25** 395305 (2013)
157. Avila J et al. *J. Phys. Condens. Matter* **25** 262001 (2013)
158. Ezawa M *J. Phys. Soc. Jpn.* **84** 121003 (2015)
159. Knox K R et al. *Phys. Rev. B* **78** 201408(R) (2008)
160. Hwang C et al. *Sci. Rep.* **2** 590 (2012)
161. Zhao J et al. *Prog. Mater. Sci.* **83** 24 (2016)
162. Li G, Andrei E Y *Nat. Phys.* **3** 623 (2007)
163. Lin C-L et al. *Phys. Rev. Lett.* **110** 076801 (2013)
164. Johnson N W et al. *Adv. Funct. Mater.* **24** 5253 (2014)
165. Cahangirov S et al. *Phys. Rev. B* **88** 035432 (2013)
166. Dávila M E, Le Lay G *Sci. Rep.* **6** 20714 (2016)
167. Ni Z et al. *Nano Lett.* **12** 113 (2012)
168. Tsai W-F et al. *Nat. Commun.* **4** 1500 (2013)
169. Qin R et al. *AIP Adv.* **2** 022159 (2012)
170. Wang Y, Ding Y *Solid State Commun.* **155** 6 (2013)
171. Huang C et al. *J. Phys. Chem. Lett.* **7** 1919 (2016)
172. Xie H et al. *Phys. Rev. B* **93** 075404 (2016)
173. Kuang Y D et al. *Nanoscale* **8** 3760 (2016)
174. Tao L et al. *Nat. Nanotechnol.* **10** 227 (2015)
175. Madhushankar B N et al. *2D Mater.* **4** 021009 (2017)
176. Tritsaris G A et al. *Nano Lett.* **13** 2258 (2013)
177. Prasongkit J et al. *J. Phys. Chem. C* **119** 16934 (2015)
178. Hussain T et al. *J. Phys. Chem. C* **120** 25256 (2016)
179. Gupta S K et al. *RSC Adv.* **6** 102264 (2016)
180. Gonzalez Szwacki N, Sadrzadeh A, Yakobson B I *Phys. Rev. Lett.* **98** 166804 (2007)
181. Zhai H-J et al. *Nat. Chem.* **6** 727 (2014)
182. Chernozatonskii L A, Sorokin P B, Yakobson B I *JETP Lett.* **87** 489 (2008); *Pis'ma Zh. Eksp. Teor. Fiz.* **87** 575 (2008)
183. Singh A K, Sadrzadeh A, Yakobson B I *Nano Lett.* **8** 1314 (2008)
184. Feng B et al. *Nat. Chem.* **8** 563 (2016)
185. Penev E et al. *Nano Lett.* **12** 2441 (2012)
186. Zhang Z et al. *Angew. Chem. Int. Ed.* **54** 13022 (2015)
187. Tang H, Ismail-Beigi S *Phys. Rev. Lett.* **99** 115501 (2007)
188. Zhao Y, Zeng S, Ni J *Appl. Phys. Lett.* **108** 242601 (2016)
189. Tang H, Ismail-Beigi S *Phys. Rev. B* **80** 134113 (2009)
190. Karmodak N, Jemmis E D *Angew. Chem. Int. Ed.* **56** 10093 (2017)
191. Liu Y, Penev E S, Yakobson B I *Angew. Chem. Int. Ed.* **52** 3156 (2013)
192. Mannix A J et al. *Science* **350** 1513 (2015)
193. Kiraly B et al. *ACS Nano* **13** 3816 (2019)
194. Liu X et al. *Nat. Commun.* **10** 1642 (2019)
195. Zhang Z et al. *Sci. Adv.* **5** eaax0246 (2019)
196. Li W et al. *Sci. Bull.* **63** 282 (2018)
197. Zhang Z et al. *Nano Lett.* **16** 6622 (2016)
198. Zhang Z, Penev E S, Yakobson B I *Chem. Soc. Rev.* **46** 6746 (2017)
199. Petö J et al. *Nat. Chem.* **10** 1246 (2018)
200. Kunstmann J, Quandt A *Phys. Rev. B* **74** 035413 (2006)
201. Tsafack T, Yakobson B I *Phys. Rev. B* **93** 165434 (2016)
202. Zhang Z et al. *Adv. Funct. Mater.* **27** 1605059 (2017)
203. Li T *Phys. Rev. B* **85** 235407 (2012)
204. Wei Q, Peng X *Appl. Phys. Lett.* **104** 251915 (2014)
205. Yang C et al. *Comput. Mater. Sci.* **95** 420 (2014)
206. Mortazavi B et al. *Phys. Chem. Chem. Phys.* **18** 27405 (2016)
207. Feng B et al. *Phys. Rev. B* **94** 041408 (2016)
208. Penev E S, Kutana A, Yakobson B I *Nano Lett.* **16** 2522 (2016)
209. Zhao Y, Zeng S, Ni J *Phys. Rev. B* **93** 014502 (2016)
210. Liao J-H et al. *Phys. Chem. Chem. Phys.* **19** 29237 (2017)
211. Gao M et al. *Phys. Rev. B* **95** 024505 (2017)
212. Li G et al. *J. Phys. Chem. C* **122** 16916 (2018)
213. Cheng C et al. *2D Mater.* **4** 025032 (2017)
214. Xiao R C et al. *Appl. Phys. Lett.* **109** 122604 (2016)
215. Er S, de Wijs G A, Brocks G *J. Phys. Chem. C* **113** 18962 (2009)
216. Kubas G J *J. Organomet. Chem.* **635** 37 (2001)
217. Bhattacharya S, Bhattacharya A, Das G P *J. Phys. Chem. C* **116** 3840 (2011)
218. Niu J, Rao B K, Jena P *Phys. Rev. Lett.* **68** 2277 (1992)
219. Jena P *J. Phys. Chem. Lett.* **2** 206 (2011)
220. Tan X, Tahini H A, Smith S C *ACS Appl. Mater. Interfaces* **9** 19825 (2017)
221. Tai T B, Nguyen M T *Chemistry Eur. J.* **19** 2942 (2013)
222. Zhang X et al. *Nanoscale* **8** 15340 (2016)
223. Jiang H R et al. *Nano Energy* **23** 97 (2016)
224. Mortazavi B et al. *J. Power Sources* **329** 456 (2016)
225. Jiang H R et al. *J. Mater. Chem. A* **6** 2107 (2018)
226. Zhang L et al. *J. Phys. Chem. C* **121** 15549 (2017)
227. Wang Z-Q et al. *Front. Phys.* **14** 33403 (2019)
228. Shi L et al. *Nanoscale* **9** 533 (2017)
229. Mir S H et al. *Appl. Phys. Lett.* **109** 053903 (2016)
230. Liu C et al. *J. Phys. Chem. C* **122** 19051 (2018)
231. Kochat V et al. *Sci. Adv.* **4** e1701373 (2018)
232. Deng J et al. *Nat. Mater.* **17** 1081 (2018)
233. Zhu F et al. *Nat. Mater.* **14** 1020 (2015)
234. Apte A et al. *2D Mater.* **6** 015013 (2018)
235. Zhu Z et al. *Phys. Rev. Lett.* **119** (2017)
236. Qin J et al. *ACS Nano* **11** 10222 (2017)
237. Xu Y et al. *Phys. Rev. Lett.* **111** 136804 (2013)
238. Rachel S, Ezawa M *Phys. Rev. B* **89** 195303 (2014)
239. Xiong W et al. *Phys. Chem. Chem. Phys.* **18** 6534 (2016)
240. Xing D-X et al. *Superlatt. Microstruct.* **103** 139 (2017)
241. Wang D et al. *Phys. Chem. Chem. Phys.* **17** 26979 (2015)
242. Lu J et al. *J. Mater. Chem.* **12** 2755 (2002)
243. Xian L et al. *2D Mater.* **4** 041003 (2017)